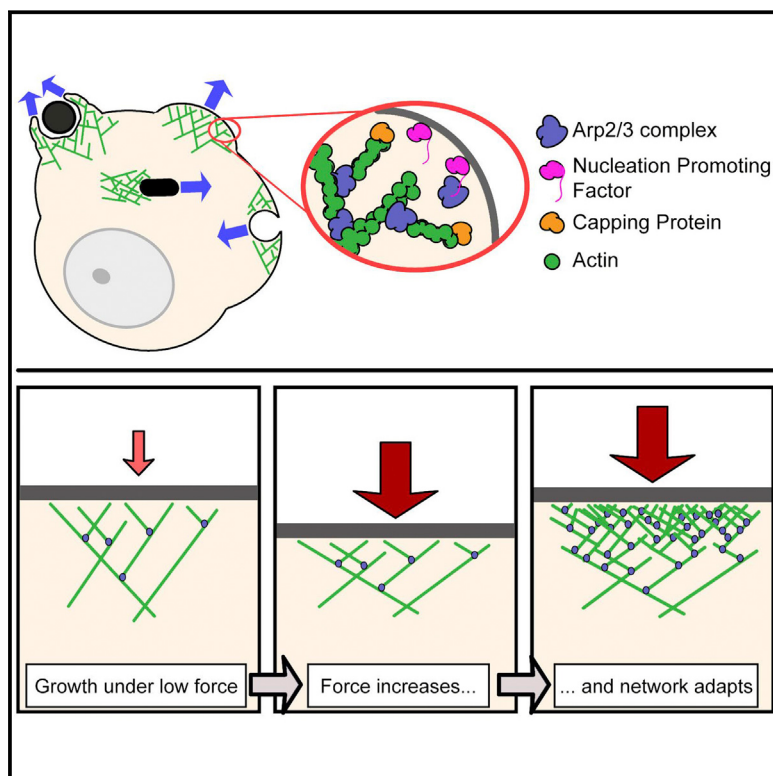


Force Feedback Controls Motor Activity and Mechanical Properties of Self-Assembling Branched Actin Networks

Graphical Abstract



Authors

Peter Bieling, Tai-De Li,
Julian Weichsel, ..., Bo Huang,
Daniel A. Fletcher, R. Dyche Mullins

Correspondence

fletch@berkeley.edu (D.A.F.),
dyche.mullins@ucsf.edu (R.D.M.)

In Brief

Force-feedback regulates the assembly and basic material properties of branched actin networks, increasing their density, stiffness, and power output, providing a “memory” of their mechanical history.

Highlights

- Force-generating actin networks adapt to changing mechanical resistance
- Resistance increases network density and power output without altering composition
- Force-feedback strengthens load-bearing networks and gives them mechanical memory
- Both external and internal material properties control network motor activity

Force Feedback Controls Motor Activity and Mechanical Properties of Self-Assembling Branched Actin Networks

Peter Bieling,^{1,2,7} Tai-De Li,^{2,3,4,7} Julian Weichsel,⁵ Ryan McGorty,⁶ Pamela Jreij,² Bo Huang,⁶ Daniel A. Fletcher,^{2,3,*} and R. Dyche Mullins^{1,*}

¹Department of Cellular and Molecular Pharmacology and Howard Hughes Medical Institute, University of California, San Francisco, Genentech Hall, 600 16th Street, San Francisco, CA 94158, USA

²Department of Bioengineering and Biophysics Program, University of California, Berkeley, 648 Stanley Hall MC 1762, Berkeley, CA 94720, USA

³Physical Biosciences Division, Lawrence Berkeley National Laboratory, 648 Stanley Hall MC 1762, Berkeley, CA 94720, USA

⁴Advance Science Research Center, City University of New York, 85 St. Nicholas Terrace, New York, NY 10031, USA

⁵Department of Chemistry, University of California, Berkeley, 207 Gilman Hall, Berkeley, CA 94720, USA

⁶Department of Biochemistry and Biophysics, University of California, San Francisco, Genentech Hall, 600 16th Street, San Francisco, CA 94158, USA

⁷Co-first author

*Correspondence: fletch@berkeley.edu (D.A.F.), dyche.mullins@ucsf.edu (R.D.M.)

<http://dx.doi.org/10.1016/j.cell.2015.11.057>

SUMMARY

Branched actin networks—created by the Arp2/3 complex, capping protein, and a nucleation promoting factor—generate and transmit forces required for many cellular processes, but their response to force is poorly understood. To address this, we assembled branched actin networks *in vitro* from purified components and used simultaneous fluorescence and atomic force microscopy to quantify their molecular composition and material properties under various forces. Remarkably, mechanical loading of these self-assembling materials increases their density, power, and efficiency. Microscopically, increased density reflects increased filament number and altered geometry but no change in average length. Macroscopically, increased density enhances network stiffness and resistance to mechanical failure beyond those of isotropic actin networks. These effects endow branched actin networks with memory of their mechanical history that shapes their material properties and motor activity. This work reveals intrinsic force feedback mechanisms by which mechanical resistance makes self-assembling actin networks stiffer, stronger, and more powerful.

INTRODUCTION

Cells are physical objects that interact with the world around them by generating, transmitting, and resisting forces (Janmey and McCulloch, 2007; Kasza et al., 2007). In eukaryotic cells, many of these forces flow through the collection of cross-linked, branched, and entangled filament networks that form the actin

cytoskeleton (Fletcher and Mullins, 2010; Pollard and Cooper, 2009). Branched actin networks, for example, generate pushing forces (Mogilner and Oster, 1996) required for many cellular processes, including protrusion of leading edge membranes in migrating cells (Bisi et al., 2013; Wu et al., 2012), motility of intracellular pathogens (Welch and Way, 2013), healing of cell ruptures (Clark et al., 2009), endocytosis (Mooren et al., 2012), phagocytosis (Insall and Machesky, 2009), and the formation of tight cell adhesions (Yamaguchi et al., 2005). These dynamic actin networks are created by the branching activity of the Arp2/3 complex, which creates new filaments from the sides of preexisting filaments (Mullins et al., 1998). In addition to the Arp2/3 complex, assembly of force-generating networks requires two accessory proteins: a WASP-family nucleation promoting factor (NPF) and a filament capping protein (Akin and Mullins, 2008). Despite the mechanical nature of their functions, we know little about how branched actin networks respond to force at the molecular or the material level (Chaudhuri et al., 2007; Marcy et al., 2004; Parekh et al., 2005; Pujol et al., 2012). Previous work focused on mechanics of isotropic actin networks held together by entanglement or cross-linking (Stricker et al., 2010), which are dominated by “entropic elasticity” of individual actin filaments (Gardel et al., 2004a; MacKintosh et al., 1995; Storm et al., 2005; Wagner et al., 2006). Theory developed from this work explains effects of “pre-stress” on actin gels (Gardel et al., 2006), but its connection to the dynamic and anisotropic cytoskeletal networks created by living cells remains unclear.

Cells construct actin networks by concentrating assembly factors at specific sites, establishing physical boundary conditions that dictate dynamics and architecture of the network. Filament nucleation and branching by the Arp2/3 complex, for example, creates actin networks that generate force to drive membrane movement (Svitkina and Borisy, 1999; Vinzenz et al., 2012; Wu et al., 2012). Because Arp2/3 activity depends on membrane-associated NPFs, new filaments are created only in a narrow

zone adjacent to the membrane. Imposing this boundary condition on filament formation produces anisotropic networks in which most growing filament ends point toward the membrane (Maly and Borisy, 2001; Weichsel et al., 2012) and has profound mechanical consequences. Isotropic networks assembled *in vitro* from soluble and randomly distributed Arp2/3 complexes are mechanically weak (Nakamura et al., 2002), while networks assembled from surface-immobilized NPFs are more coherent and much stiffer (Chaudhuri et al., 2007; Marcy et al., 2004). Once polarized, growing actin networks encounter obstacles and experience external forces that may affect their assembly.

Here, we ask how mechanical forces affect the biochemical interactions that underlie network assembly, and we investigate how the mechanical history of self-assembling networks affects their material properties and motor activity. To measure molecular and mechanical responses of branched actin networks to force, we applied simultaneous total internal reflection fluorescence (TIRF) and atomic force microscopy (AFM) to actin networks assembled from purified components. To create biologically relevant boundary conditions for network growth, we micro-patterned the surface of glass coverslips with a WASP-family NPF. We then quantified incorporation of proteins into growing networks by TIRF microscopy. At the same time, we used an AFM cantilever to apply force and quantify network growth velocity. To understand the functional consequences of biochemical responses to force, we also used the AFM cantilever to measure material properties of branched actin networks grown under different physical and biochemical conditions.

We find that force fundamentally alters the assembly, architecture, and function of branched actin networks: growth velocity decreases while filament density increases in response to force. Microscopically, the increase in filament density reflects two changes: (1) greater number of pushing filaments, and (2) tighter filament packing. Average filament length, however, does not change with force. Interestingly, the fractional energy of polymerization converted into mechanical work increases with applied force. Macroscopically, force on growing actin networks enhances their stiffness and mechanical resilience. Networks exhibit their maximum stiffness when loaded with the same forces they experienced during growth. These force-induced changes in material properties, however, do not scale with density or stress according to “universal” laws derived for isotropic actin gels (Gardel et al., 2004b, 2006). This argues that the physics of Arp2/3-generated actin networks differs fundamentally from that of random, cross-linked networks. Furthermore, we find that assembling branched actin networks under changing load forces produces materials whose stiffness and force-velocity relationships are dominated by their loading history rather than molecular composition.

RESULTS

Assembly of Branched Actin Networks with Physiologically Relevant Boundary Conditions

To mimic enrichment of WASP-family NPFs on cellular membranes, we immobilized the Arp2/3-activating region of WAVE1 on functionalized coverslips (Fourniol et al., 2014) (Figure 1A). We then added purified components—monomeric actin, Arp2/

3 complex, and capping protein (CP)—to the WAVE1ΔN patterns to create polarized actin networks. To prevent spontaneous nucleation, we also added the actin-binding protein profilin (Pantaloni and Carlier, 1993; Tilney et al., 1983). By confocal fluorescence microscopy, networks formed three-dimensional “pillars” growing from WAVE1ΔN-coated squares (Figure 1B) at $7.33 \pm 1.61 \mu\text{m}/\text{min}$ (Figure S1A), at a rate comparable to actin assembly at the leading edge of migrating cells (Renkawitz et al., 2009). Growth velocity did not strongly depend on NPF pattern size, indicating that network assembly is not limited by diffusion (Figure S1B). Because <0.01% of the coverslip is coated with the NPF, network growth did not significantly deplete the pool of soluble protein components, and the filament networks grew with constant density and velocity for more than an hour (Figure S1C). The distribution of fluorescent Arp2/3 (not shown) and CP (Figures 1C and 1D) were also homogeneous throughout the networks.

We used TIRF microscopy to quantify the rate at which individual molecules of actin, CP, and Arp2/3 join the growing network at the NPF-coated surface. We reduced the fraction of labeled actin to 1 in 1.5×10^6 molecules, which enabled us to visualize incorporation of individual actin monomers into the network. Each incorporation event was marked by the sudden appearance of a fluorescent spot within an NPF square (Figure 1E, top panel) that subsequently decayed exponentially with time as the molecule moved with the growing network out of the evanescent excitation field (Figures 1E and S1D; Movie S1; Supplemental Experimental Procedures). We counted single-molecule binding events and then divided their frequency by the actin labeling ratio to compute a total polymerization rate of $7,135 \text{ actin monomers} \cdot \text{s}^{-1} \cdot \mu\text{m}^{-2}$ under our experimental conditions.

Using this single-molecule approach, we also determined the total rates of nucleation/branching ($68 \text{ Arp2/3} \cdot \text{s}^{-1} \cdot \mu\text{m}^{-2}$) and capping ($57 \text{ CP} \cdot \text{s}^{-1} \cdot \mu\text{m}^{-2}$; Figure 1E, middle and bottom). The similarity of these rates indicates that most growing filament ends generated by NPF-stimulated Arp2/3 activity at the cover-slip surface are also capped near this surface, within the shallow TIRF illumination field. We calculated the average filament length in two ways: by the ratio of polymerization rate to the rate of nucleation or capping (Figure 1F) and found that our filaments grew to a mean length of ~300 nm (or 110 monomers), similar to filament lengths observed in branched networks *in vivo* (Vinzienz et al., 2012). We conclude that our reconstituted system captures the basic architecture and assembly dynamics of cellular actin networks.

Effect of Load on Branched Actin Network Velocity, Density, and Efficiency

To measure network growth and to apply compressive forces, we positioned an AFM cantilever over an NPF-coated square before initiating network assembly (Figure 2A). To apply constant force to a growing network, we used optical feedback to maintain constant deflection of the AFM cantilever. We divide the cantilever force by the cross-sectional area of the actin network ($200 \mu\text{m}^2$) and report our measurements as force per unit area or stress ($\text{pN}/\mu\text{m}^2$ or equivalently, Pa). We first applied a step-wise series of increasing load forces to a growing network and measured steady-state growth velocity after the network

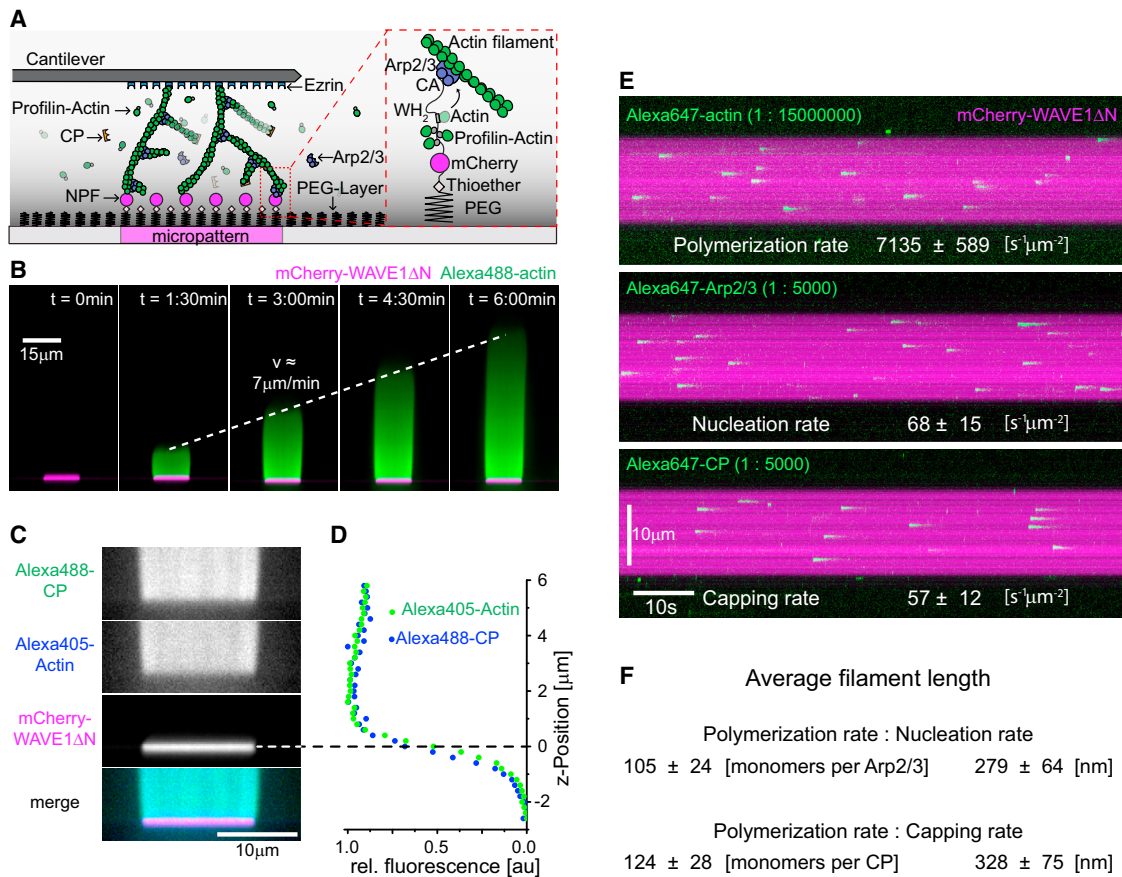


Figure 1. Reconstitution of Branched Network with In-Vivo-like Properties from Micropatterned Surfaces

(A) Scheme: NPF patches, bound to a PEG passivated coverslip, rapidly assemble dendritic networks from profilin-actin, CP and Arp2/3. Networks are visualized by fluorescence microscopy and mechanically manipulated through an AFM cantilever.

(B) Confocal microscopy (reconstructed axial view) of actin assembly (Alexa488-actin, green) from WAVE1ΔN micropatterns (magenta) after indicated time of protein addition (5 μM actin [1% Alexa 488-labeled], 5 μM profilin, 100 nM Arp2/3, 100 nM CP).

(C) Reconstructed axial view for indicated dendritic network components from confocal imaging. Conditions as in (B) with 15% TMR-CP and 5% Alexa647-Arp2/3.

(D) Intensity profiles of actin (blue) and CP (green) along axial dimension from confocal microscopy. Surface position ($z = 0$) was defined by the maximal mCherry-WAVE1 fluorescence signal (dashed line).

(E) Space-time plots (kymographs) from single molecule TIRF imaging of either actin (top), Arp2/3 (middle), or CP (bottom) incorporation into dendritic networks at a small reference stress of 25 pN/μm². Rates were determined by the product of the incorporation rate and the known labeling ratio (see [Supplemental Experimental Procedures](#)).

(F) Average filament lengths as determined by the ratio of the single-molecule polymerization and the nucleation (top) or the capping (bottom) rate. All error indicators are SEM.

See also [Figure S1](#) and [Movie S1](#).

adapted to the new growth force ([Figure S2](#)). This steady-state growth velocity fell sharply under small loads ([Figure 2B](#)) but did not stall completely until the load exceeded 1,250 pN/μm², a value comparable to pushing and pulling stresses generated by crawling cells ([Gardel et al., 2008; Prass et al., 2006](#)). The new steady-state growth velocity did not depend on previous forces ([Figure S3](#)), indicating that instantaneous force alone determines network growth at steady state. Finally, the force velocity curve does not follow a simple exponential decay as expected for a fixed number of growing filaments by Elastic Brownian Ratchet models ([Peskin et al., 1993](#)). Instead, velocity falls sharply at low force but decreases more gradually at higher

force ([Figure 2B](#)), suggesting a possible load-dependent effect on filament density.

To determine the effect of force on filament density, we performed TIRFM of fluorescent actin incorporating into networks growing under load ([Figure 2C](#)). While growth velocity decreases with applied load, the density of actin filaments in the network increases strongly ([Figures 2D, 2E, and S3; Movie S2](#)). This increased filament density does not reflect elastic compression but rather stable, force-induced changes in the material (see next section). The fall in growth velocity and the rise in filament density nearly compensate each other, adding up to a surprisingly weak, load-dependent decrease in the rate of actin

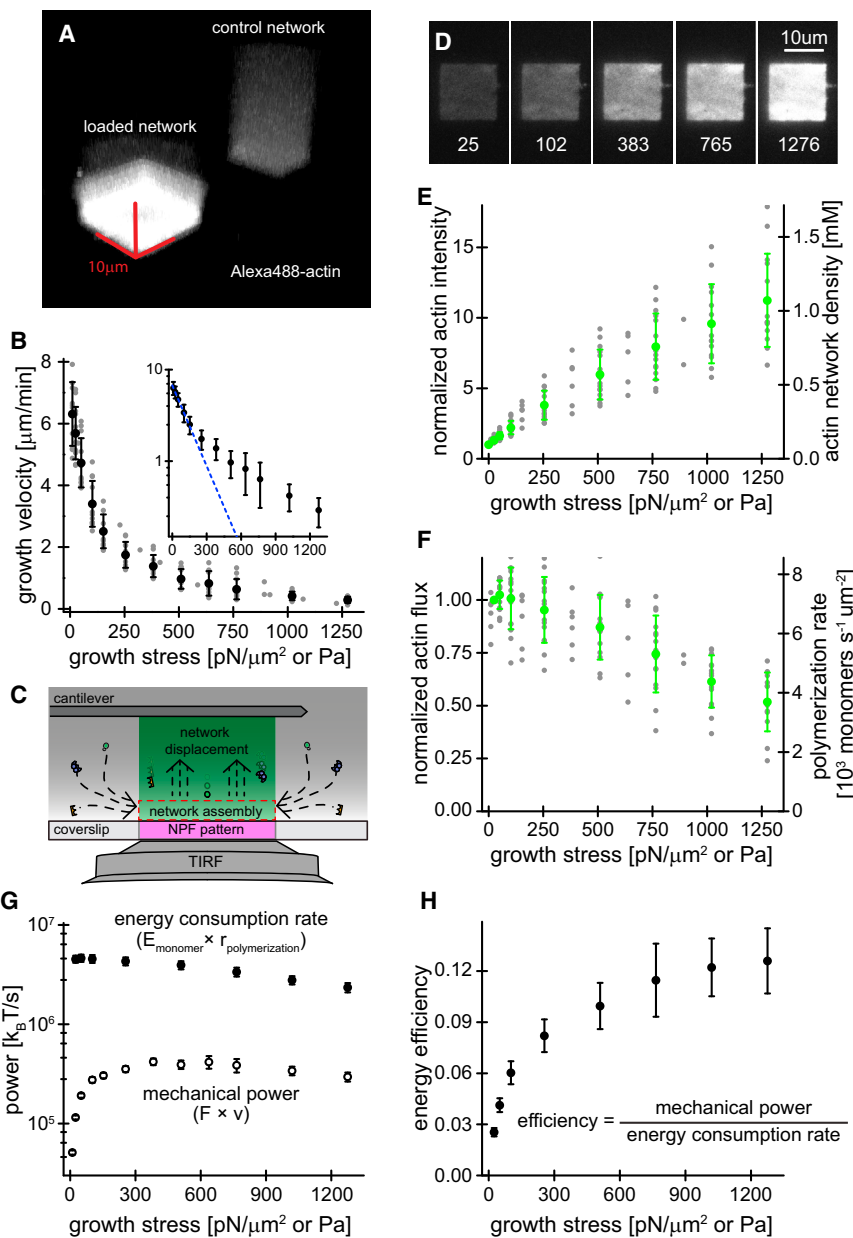


Figure 2. Force-Feedback Increases Density and Mechanical Efficiency of Branched Actin Networks

(A) Three-dimensional reconstruction from confocal microscopy of two networks growing under an AFM cantilever (left) or freely into solution (right).

(B) Steady-state growth velocities of networks as a function of growth stress. Grey, raw data; black, averages. Inset: semi-logarithmic replot together with a single exponential fit (dashed blue line) to the low-force data. Error bars are SD.

(C) Scheme of network assembly visualized by TIRFM.

(D) TIRFM images of networks (Alexa488-actin) at indicated growth stress.

(E) Actin intensity (left y axis, normalized to unloaded control) and the calculated actin density (right y axis, calibrated by single molecule experiments (Figure 1E; Experimental Procedures) as a function of growth stress. Grey, raw data; green, averages. Error bars are SD.

(F) Actin flux (left y axis, product of network density, see Figure 2B, and growth velocity, see Figure 2C, normalized to flux at 25 $\text{pN}/\mu\text{m}^2$) and polymerization rates (right y axis, calibrated by single molecule experiments [see Figure 1E] as a function of growth stress. Grey, raw data; green, averages. Error bars are SD.

(G) Semi-logarithmic plot of energy consumption rate (product of polymerization rate ($r_{\text{polymerization}}$, Figure 2F) and free energy change per monomer ($E_{\text{monomer}} = 3.18 \text{ k}_B T$; see Supplemental Experimental Procedures) and mechanical power (calculated by the product of velocity (v) and force (F), see Figure 2E) as a function of growth stress. Error bars are SEM.

(H) Mean energy efficiency (determined by the ratio of the mechanical power and the energy consumption rate, see Figure 2G) as a function of growth stress. Error bars are SEM. See also Figures S2 and S3 and Movie S2.

incorporation (flux) into the network (Figure 2F). Using our single-molecule measurement of actin polymerization under low growth force (Figure 1E) as calibration, we calculated assembly rates and filament densities for networks grown under other loading conditions (right y axes, Figures 2F and 2E). Over the functional force range—from zero load to network stall—filament concentration in the network increases from 0.125 mM to 1 mM (filament volume fractions of 0.5%–3.7%).

From basic thermodynamics (Hill and Kirschner, 1982), we estimated the free energy change of one actin monomer adding to the barbed end of a filament under our experimental conditions (Supplemental Experimental Procedures). Multiplying this value by the actin flux yields the rate of energy consumption by the network as it pushes against various loads (Figure 2G). We

used the force-velocity relationship of our branched networks (Figure 2B) to calculate the mechanical power output (product of force and growth velocity) at each force (Figure 2G). The ratio of the power output to the energy consumption rate yields the efficiency of the branched actin network as a motor (Figure 2H). This efficiency turns out to be highly load-dependent, increasing from ~3% at low force to ~14% at high force. Thus, polymerizing filaments appear to share their burden more evenly under high load, with fewer futile polymerization events occurring away from the network/load boundary.

Architecture and Assembly Kinetics of Branched Networks Adapt to Load

We find that force increases filament density in branched actin networks, but does this reflect (1) more polymerizing filaments, (2) a shift in network microstructure to denser packing, or (3) both (Figure 3A)? To determine whether load increases

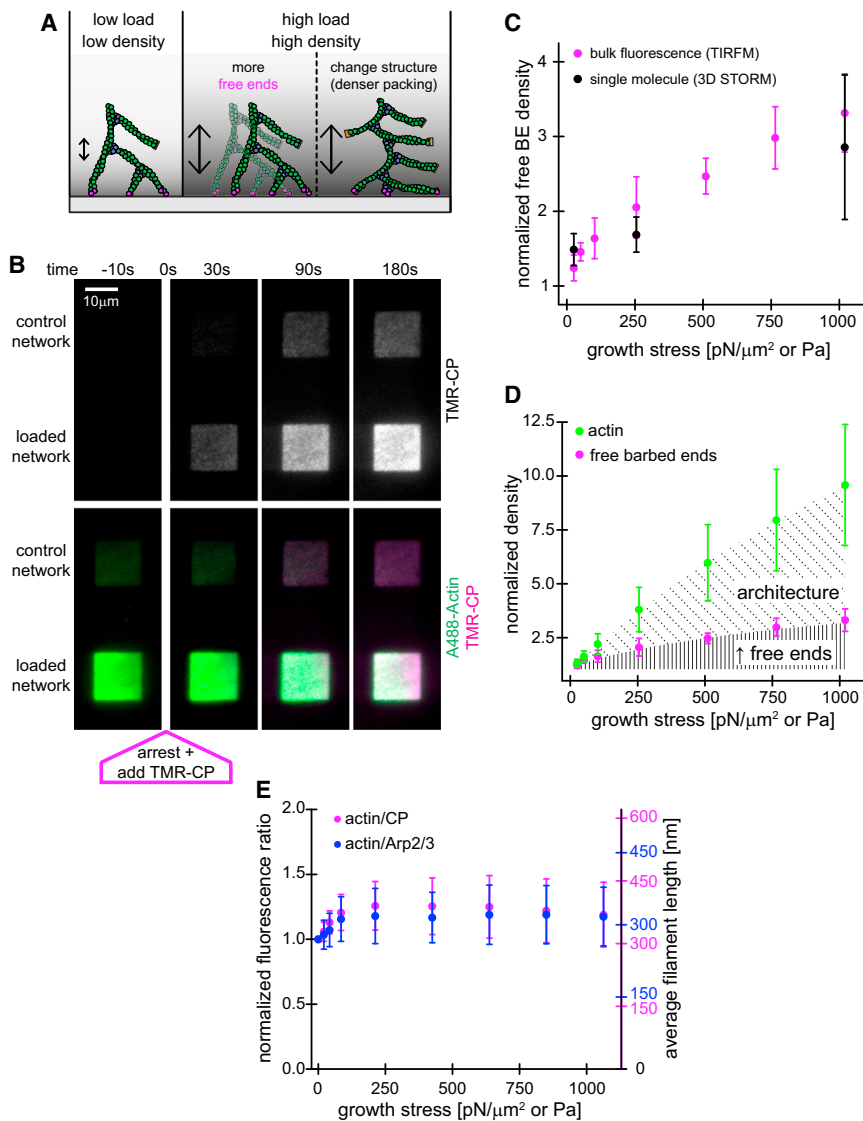


Figure 3. Force-Feedback Increases the Density of Free Barbed Ends within the Network but Does Not Alter the Stoichiometry of Its Constituents

(A) Scheme of network assembly under low (left) or high stress (middle and right). Density increase by either rise in the number of free ends (middle) and/or changes in packing of filaments (right).

(B) TIRFM images of TMR-CP binding (top alone [greyscale] or as color merge with Alexa488-actin [green and magenta, bottom]) to networks either unloaded or assembled under 1,020 pN/ μm^2 load at indicated times after kinetic arrest ($t = 0$ is the addition of labeling mix [27.5 μM Latrunculin B, 27.5 μM phalloidin, 18.5 nM TMR-CP]).

(C) Free barbed end densities (normalized to unloaded control) from either TIRFM (magenta) or 3D STORM (black) as a function of growth stress.

(D) Free barbed end (magenta) or actin (green) densities normalized to unloaded control as a function of growth stress. The increased free end density (vertical, solid lines) accounts for a fraction of actin density rise and the residual rise is due to denser filament packing (diagonal, dotted lines).

(E) Ratio of fluorescence intensities (left y axis, normalized to unloaded control) or average filament lengths (right y axis, calibrated by single molecule assays, Figure 1F) of actin/CP (magenta) or actin/Arp2/3 (blue) as a function of growth stress. Error bars are SD.

See also Figures S4 and S5 and Movie S3.

the number of polymerizing filaments, we developed an “arrest-and-label” method to visualize free filament ends in the network (Figure S4). Briefly, we assembled two dendritic networks side-by-side: one unloaded and one growing against defined load. We then arrested network assembly by adding Phalloidin and Latrunculin B, together with a fluorescent derivative of CP (Figure 3B). The two small-molecules rapidly freeze actin dynamics (Akin and Mullins, 2008), while the fluorescent CP labels free barbed ends of filaments in the network (Figures 3B and S4; Movie S3). Accumulation of labeled CP was biphasic (Figures S4D and S4E; Supplemental Experimental Procedures), with rapid binding to free barbed ends followed by a very slow exchange of labeled CP with unlabeled CP throughout the network (Reymann et al., 2011; Schafer et al., 1996). In addition to TIRFM, we used three-dimensional stochastic optical reconstruction microscopy (3D-STORM) (Huang et al., 2008) (Supplemental Experimental Procedures) to count free barbed ends in the network. The use of 3D-STORM enabled us to rule out potential

TIRF artifacts, such as compression of free ends into the evanescent field (Figure S5). Both TIRF and 3D-STORM imaging of fluorescent CP after growth arrest showed that the number of free barbed ends in the dendritic network increases strongly (~3.3-fold) with force (Figure 3C).

To estimate the absolute number of free barbed ends, we combined these data with single-molecule measurements of actin incorporation. Based on the growth velocity of our networks under low force (7.33 $\mu\text{m}/\text{min}$, Figure S1), we estimate one free barbed end grows by ~46 monomers per second, which implies the existence of ~160 growing filament ends/ μm^2 under low force. This number increases to ~550/ μm^2 at high load forces near stall. If growing barbed ends share this load equally, then each polymerizing filament generates 1.9 pN of force under high loads. This greater number of growing filaments only partly accounts for the observed increase in filament density under load (Figure 3D), suggesting that micro-structural changes also occur in the network.

Since force causes changes in filament number and geometry we looked for other force-induced effects on network architecture, including changes in filament length. As above, we calculated average filament length in two ways, from the ratio of fluorescent Arp2/3 complex (on pointed ends) and CP (on barbed ends) to polymeric actin in the network (Figure 3F), which

we calibrated with our single-molecule measurements of CP, Arp2/3 complex, and actin incorporating into networks under low force (Figures 1E and 1F). Remarkably, these measurements reveal that the mean filament length in a branched actin network remains constant from low loads that have little effect on network growth up to high loads that almost cause them to stall (Figure 3F). These results suggest that robustness of network stoichiometry under load reflects a close match between the force responses of filament elongation and capping.

Mechanics of Branched Actin Networks Depends on the Force Experienced during Growth

How do load-induced changes in network architecture affect the ability of branched networks to transmit and resist forces? To address this question, we used AFM-based micro-rheometry to probe the material properties of branched actin networks grown under various loads (Figure 4A). We assembled networks under a constant growth force and arrested their assembly at a height of 10 μm with Latrunculin B. The slow dissociation of CP (Schafer et al., 1996) and the Arp2/3 complex (Beltzner and Pollard, 2008) from branched filaments ensured that networks remain essentially constant during the time required to measure their material properties (Figure S6A; Experimental Procedures). After assembly under load and kinetic arrest, we performed AFM micro-rheometry on networks at a small, constant force (12.5–25 pN/ μm^2). Under these “relaxed” conditions we measured elasticity in the range of 10³–10⁴ Pa, consistent with previous measurements on branched networks (Chaudhuri et al., 2007; Marcy et al., 2004; Pujol et al., 2012) (Figure 4B). Both the elastic (Figure 4B) and viscous moduli (Figure S6C) increased with increasing growth force, a change that corresponded to increased filament density. Interestingly, when we removed the growth force immediately following arrest, the height of the network increased only slightly ($\leq 10\%$, Figure 4C), regardless of the magnitude of the force. This minimal height change shows that force-dependent increases in actin density are stored in the micro-architecture of the network and are not the result of elastic compression.

Branched Actin Networks Are Maximally Elastic and Minimally Viscous under Loads that Match Their Original Growth Force

Many biological polymer networks assembled in the absence of force exhibit strong stiffening when subjected to subsequent loads or “pre-stress” (Gardel et al., 2006; Janmey et al., 1991; Storm et al., 2005). To investigate the mechanical response of branched networks, we performed rheology measurements on growth-arrested actin networks assembled at various growth forces and subsequently pre-stressed with a range of “test loads” (Figures 4D and S7). We find that branched actin networks are stiffest when the test load matches the original growth force experienced during its assembly. When tested at loads above or below the original growth force, the material either becomes softer or remains the same (Figure 4E). Sparse networks assembled at low growth forces exhibit little softening at lower test loads, while denser networks assembled under high growth forces soften more significantly (4-fold) (Figure 4E). Similarly, when loaded beyond the growth force, the stiffness of

sparse networks remained relatively constant, while dense networks softened. To better compare the behavior of branched networks assembled at different growth forces, we normalized the applied test load by the original growth force. We also normalized the elasticity measured under high test-loads by the initial elasticity of the “relaxed” material. The normalized data illustrate that maximum stiffness occurs when the test load equals the growth force (Figure 4F). Interestingly, the viscous modulus of branched actin networks falls to a minimum when the test load equals the growth force, and increases at lower and higher test loads (Figures 4G and 4H). These data reveal that growing branched actin networks adapt to a specific growth force to become maximally stiff and minimally viscous at that load.

Loading Branched Networks beyond Their Growth Force Results in Mechanical Failure

We next measured recovery of the height of self-assembled actin networks following release of a test load (Figure 5A). Purely elastic materials recover 100% of their original height after force release, but we found that branched actin networks show load-dependent, irreversible height loss following high loads (Figure 5B). Such irreversible plastic deformation is analogous to crushing of a material such as Styrofoam and usually reflects permanent micro-structural changes in the material. Networks assembled under high growth forces are stiffer and more resilient to deformation compared to networks grown under low load. Normalizing the test load by the growth force causes all of our deformation data to collapse onto a single curve (Figure 5C) and reveals that the growth force also defines a critical point beyond which the material irreversibly changes. Structural failure was also evident when we measured network elasticity. When subjected to test loads below the growth force, network stiffness recovered to nearly its original value upon test load release. Once loading exceeded the growth force, however, the network failed to recover its original elasticity (Figures 5D and 5E). Such irreversible changes could affect the growth rate and elastic properties of branched actin networks exposed to varying physical boundary conditions.

Time-Varying Forces Create Inhomogeneous Actin Networks with Composite Properties

In vivo actin networks experience changing forces in a complex and heterogeneous environment. Applying such time-varying forces to growing actin networks yields inhomogeneous materials, with layers of different filament density. To study such inhomogeneous materials we assembled branched networks under changing growth forces, arrested their assembly, and measured their elasticity under varying test loads. To create two-layered networks, we first assembled a dense network under 500 pN/ μm^2 (Figure 5F, left). At a height of 4 μm , we reduced the load to 25 pN/ μm^2 (Figure 5F, right) and assembled an additional 6 μm of sparser network. We compared the mechanics of this bi-layered material to homogeneous networks assembled under high or low force alone (Figure 5G). If the bi-layered network was purely elastic its stiffness would be dominated by the weaker material (Figure 5G, dashed magenta line; Supplemental Experimental Procedures). Instead, as the test load

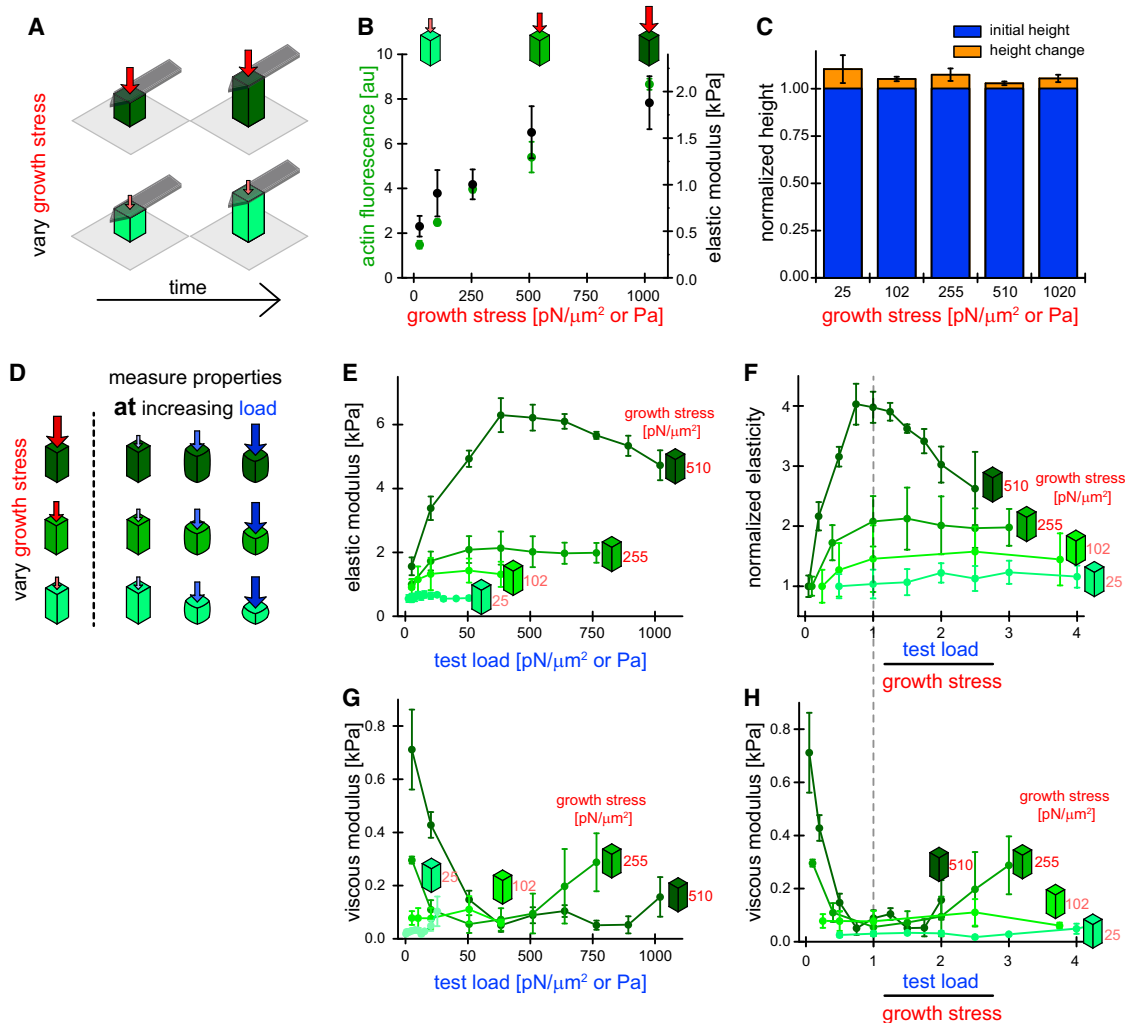


Figure 4. Adaptation to Load- and Growth-Forces Shapes the Material Properties of Branched Networks

(A) Scheme of network assembly under high (dark red arrow, top) or low (light red arrow, bottom) growth stress, resulting in high (dark green) or low (light green) network density.

(B) Actin fluorescence from TIRFM imaging (green, left y axis) and initial elasticity from micro-rheology (black, right y axis) as a function of growth stress. Measurements were performed at low test load ($12.5-25 \text{ pN}/\mu\text{m}^2$) following network arrest. Error bars are SD.

(C) Change in network height (orange) after growth stress release to low levels ($12.5-25 \text{ pN}/\mu\text{m}^2$) following arrest for networks assembled at different growth stresses as indicated. Height was normalized to the initial network height at the moment of growth arrest (blue). Error bars are SD.

(D) Scheme: networks are assembled under growth stresses (red arrows, left), arrested (dashed line) and then subjected to increasing test load (blue arrows, right). Elasticity is measured at each test load. Error bars are one-half SD.

(E) Network elasticity as a function of test load for networks assembled at different growth stresses as indicated. Error bars are one-half SD.

(F) Same as (E) with elasticity normalized to the initial elasticity and the test load normalized to the growth stress. Error bars are one-half SD.

(G) Network viscosity as a function of test load for networks assembled under different growth stresses as indicated. Error bars are one-half SD.

(H) Same as (G) but with the test load normalized to the growth stress. Error bars are one-half SD.

See also Figures S6 and S7.

approached the higher growth force, we observed stiffening in the inhomogeneous material that was intermediate between those of the high- and low-density materials (Figure 5G, middle green line). This result is explained entirely by plastic deformation of the low-density layer when test load exceeds its growth force (Figure 5G, solid magenta line; **Supplemental Experimental Procedures**). Once the weaker layer is crushed, the properties of the composite shift toward those of the denser material. In this way,

mechanical failure may enable inhomogeneous actin networks to adapt more quickly to high load forces.

Anisotropic, Branched Actin Networks Behave Differently Than Isotropic, Crosslinked Networks

The stiffness of random, isotropic actin networks (both cross-linked or entangled) scales roughly as the square of filament density (Figure 6A) (Gardel et al., 2003). We wondered whether the

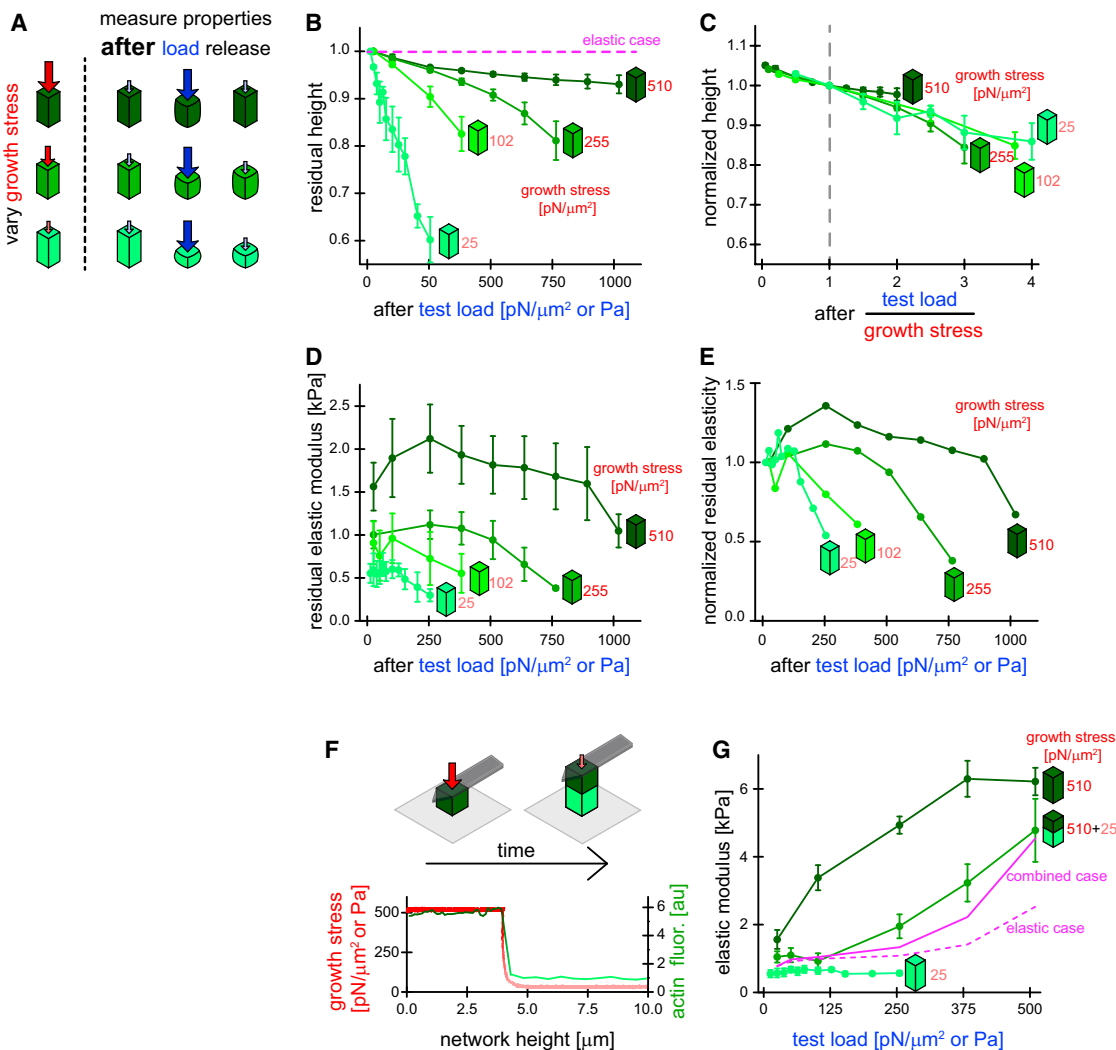


Figure 5. Loading beyond the Growth Force Causes Mechanical Failure Leading to History-Dependent Mechanical Properties

(A) Scheme: networks are assembled at different growth stresses (red arrow, left) resulting in different network densities (green), arrested (dashed line) and initial height and elasticity are measured under low test load. Networks are then subjected to stress cycles consisting of high test load followed by a low test load, recovery step during which the residual height and elasticity is determined (blue arrows, right).

(B) Residual network height (normalized to the initial height) measured during the recovery step as a function of the previously applied high test load for networks assembled under different growth stress. The dashed magenta line is the ideal elastic case (full recovery).

(C) Same as (B) but with the test load normalized to the growth stress. Residual network height was normalized to the residual height after the test load reached the growth stress.

(D) Residual network elasticity measured during the recovery step as a function of the previously applied high test load for networks assembled under different growth stresses.

(E) Same as (D) but with the residual elasticity normalized to the initial elasticity.

(F) Top: composite network assembly. Networks are first assembled at a high growth stress, i.e., at high actin density (left). Upon reaching a defined height, growth stress is reduced giving rise to a sparse network layer (right). Bottom: growth stress (red, left y axis) and actin fluorescence (green, right y axis) of a discontinuous, two-layered network as a function of network height.

(G) Network elasticity as a function of test load for either homogenous networks assembled at constant growth stress (510 or 25 pN/ μm^2) or a composite network assembled at 510 and 25 pN/ μm^2 as indicated. Dashed magenta line is the estimated network elasticity for the composite network assuming purely elastic behavior (Experimental Procedures). The continuous magenta line is an estimate that additionally includes mechanical failure (plastic deformation) (Experimental Procedures). All error bars are one-half SD.

same characteristic power-law scaling of stiffness with density describes anisotropic, branched actin networks assembled under load. Comparing our results with published data, we find that branched networks generated by localized activity of the

Arp2/3 complex are much denser and stiffer than isotropic actin networks (Figure 6A). Their elastic modulus, however, scales much more weakly with filament density ($\sim c_A^{0.6}$, where c_A is the concentration of filamentous actin). Previous studies have

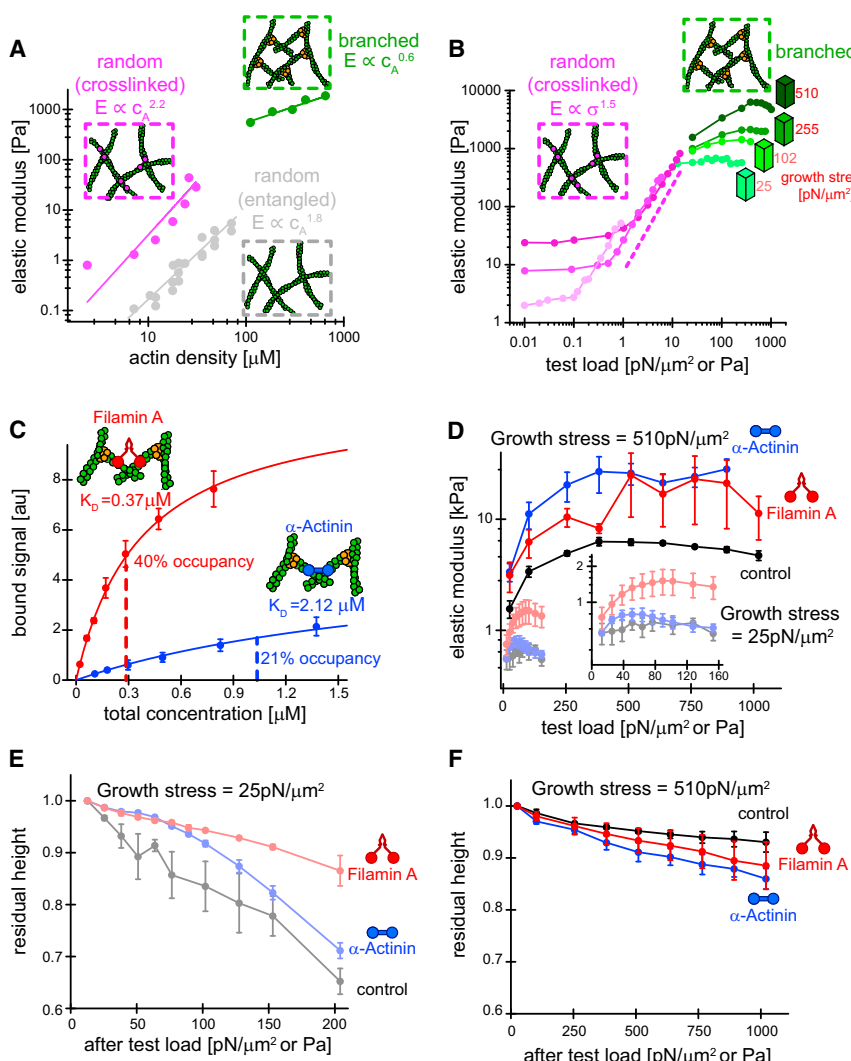


Figure 6. Branched Network Mechanics Are Distinct from Random Gels and Not Fundamentally Changed by Crosslinkers

(A) Elasticity of entangled (light gray, from Gardel et al., 2003) or crosslinked random gels (dark gray, from Gardel et al. [2004a], 0.03 actin:scrulin ratio) compared to branched networks (green) as a function of actin density. Lines are power laws with indicated scaling factors (Experimental Procedures).

(B) Double-logarithmic plot of network elasticity as a function of test load (prestress) for either random cross-linked networks of different actin concentration (magenta, from dark to light = 29.4, 21.4, 8.33 μM , 0.03 actin:scrulin ratio, from Gardel et al. [2004b]) or branched networks assembled at indicated growth stress (green). The dashed magenta line indicates the “universal” scaling behavior of random actin gels.

(C) Fluorescence of network-bound filamin-A (red) or α -actinin (blue) by confocal microscopy as a function of total concentration. Lines are fits to single-site binding models. Dashed lines indicate concentrations used for mechanical measurements resulting in a fractional occupancy of binding sites as indicated.

(D) Network elasticity as a function of test load for networks assembled at a growth stress of 25 (light) or 510 $\text{pN}/\mu\text{m}^2$ (dark) growth stress and additionally crosslinked with either filamin-A (red) or α -actinin (blue) or a buffer control (black). The dashed magenta line indicates the “universal” scaling behavior of random actin gels.

(E) Residual network height (normalized to initial network height) for networks assembled at low ($25 \text{ pN}/\mu\text{m}^2$) growth stress, crosslinked with filamin-A (red), α -actinin (blue) or a buffer control (black) as a function of the previously applied test load. Height was measured during the recovery step.

(F) Same as (E) but for networks assembled at high ($510 \text{ pN}/\mu\text{m}^2$) growth stress. All error bars are one-half SD.

also suggested that stress-induced stiffening of isotropic actin networks follows a “universal” power law, in which the elastic modulus increases as the ~ 1.5 power of the “pre-stress.” We find that, while branched actin networks exhibit stress-stiffening, this behavior does not match that of isotropic networks and does not follow a single power law across all network densities. Moreover, we observe branched network stiffening at forces more than an order of magnitude beyond the point of isotropic network failure (Figure 6B). The physics of branched actin networks, therefore, appears to be distinct from that of random gels.

Filament Crosslinking Proteins Stiffen Branched Actin Networks but Do Not Shift the Critical Force that Defines Their Material Properties

Actin filament crosslinkers filamin-A and α -actinin are thought to strengthen some branched actin networks *in vivo* (Flanagan et al., 2001; Vinzenz et al., 2012). We investigated the effect of these crosslinkers by growing branched actin networks under constant force, terminating their growth with latrunculin B, and

then adding either filamin-A or α -actinin. By visualizing labeled crosslinkers with confocal microscopy, we determined the affinities of filamin-A and α -actinin for branched actin networks to be $K_D = 0.37 \mu\text{M}$ and $2.12 \mu\text{M}$, respectively (Figure 6C), in agreement with previous studies (Nakamura et al., 2007; Wachsstock et al., 1993). Both crosslinkers stiffened branched networks (Figure 6D), but we observed interesting differences between them (Figure 6D). Dense actin networks assembled under high forces stiffened more when crosslinked by α -actinin than by filamin-A, while sparse networks assembled under low load showed the opposite behavior (Figure 6D, inset). Neither crosslinker qualitatively changed the shape of the stress-stiffening curve, indicating that the mechanical response of branched actin networks is dominated by their load-adaptive architecture rather than by properties of the crosslinker. Interestingly, filamin-A and α -actinin also produced different effects on plastic deformation of branched actin networks loaded above their growth force. Both crosslinkers protected sparse networks from plastic deformation, but α -actinin provided less protection than filamin-A

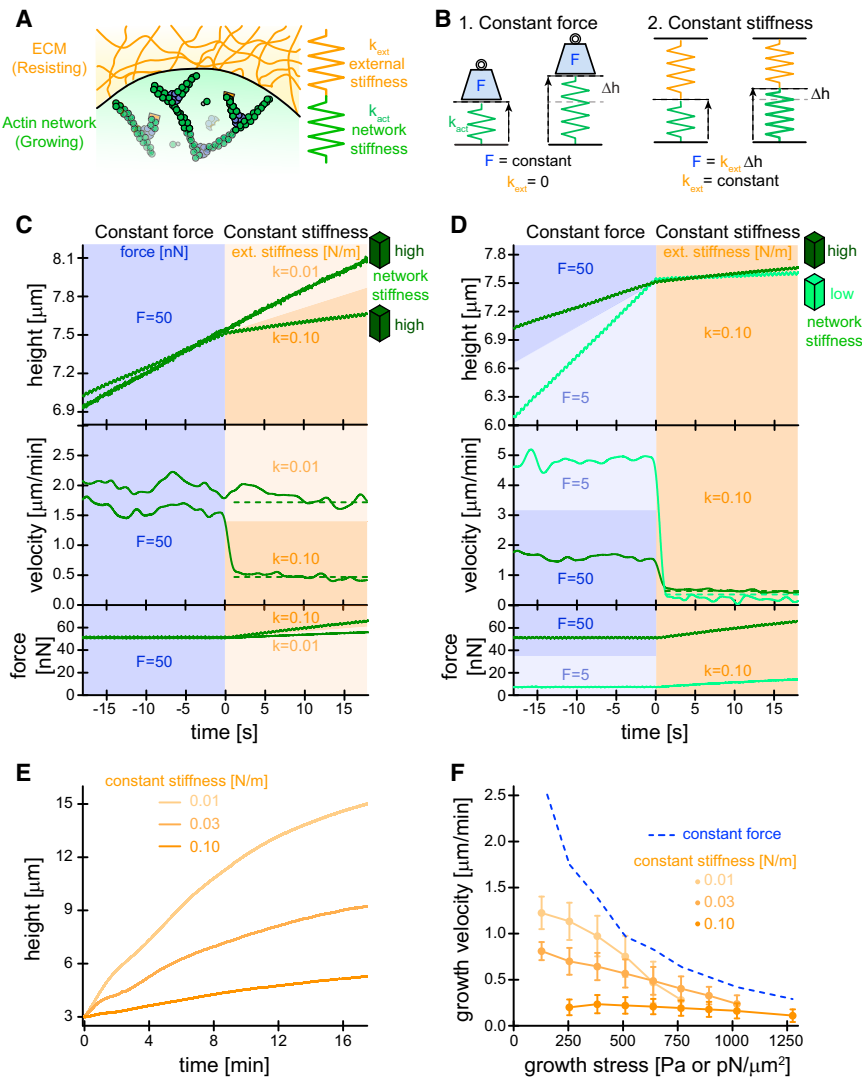


Figure 7. Branched Network Motor Activity Depends on the Mechanical Environment

(A) Scheme of branched actin networks (green) pushing against the ECM (orange) at the leading edge.

(B) Scheme of a network pushing against an AFM cantilever. The AFM can operate either keeping the force constant (zero external stiffness, left) or the external stiffness constant (defined force at a given cantilever deflection, right).

(C) Sample height (top), normalized growth velocity (middle), and force (bottom) for two networks assembled under constant high (50 nN) growth force (blue area), resulting in high (dark green traces) network stiffness. At $t = 0$, force-feedback is disengaged and networks displace cantilevers imposing either high ($k = 0.1$ N/m, dark orange area) or low ($k = 0.01$ N/m, light orange area) external stiffness. The drop in velocity can be predicted (dashed lines) from the known network stiffness (Experimental Procedures).

(D) Same as (C) for two networks grown under constant high (50 nN, dark blue area) or low (5 nN, light blue area) growth force (light blue area), resulting in high (dark green trace) and low (light green trace) network stiffness, respectively. After disengaging the force-feedback, networks are challenged with the same external cantilever stiffness ($k = 0.1$ N/m, dark orange area).

(E) Sample height as a function of time for networks pushing against cantilevers of different stiffness. Networks were grown in the absence of force to a height of 3 μm before cantilever contact ($t = 0$).

(F) Network growth velocity as a function of growth force under either constant force (blue dashed line, see Figure 2E) or constant stiffness conditions (orange) for three different external (cantilever) stiffness as indicated. Error bars are SD.

(Figure 6E). Conversely, both crosslinkers increased plastic deformation of denser networks, probably by “locking in” filament contacts induced by compression. Under these conditions, α -actinin enhanced deformation more than filamin-A (Figure 6F).

Motor Activity of Branched Actin Networks Depends on Loading History

What happens when a growing actin network pushes against a material with a defined stiffness rather than against a constant force? The extracellular matrix, for example, can offer defined mechanical resistance to actin-driven pseudopod extension (Figure 7A). A network growing against a barrier of defined stiffness does not feel constant force, but a steadily increasing force that depends on how far the barrier is displaced. We, therefore, compared the velocities of branched actin networks grown against AFM cantilevers whose deflection was controlled in two different ways. In one experiment, we applied a constant force (as before) by moving the cantilever base along with the

growing network maintaining constant cantilever deflection (Figure 7B, left). Under these conditions, force on the network does not depend on network height. In the second experiment, the cantilever base remains stationary and deflection increases as the network grows (Figure 7B, right). In this mode, the cantilever mimics a Hookean spring or an elastic material with a constant stiffness. The more the cantilever is deflected, the more force it exerts. To investigate how network growth responds to changing mechanical constraints we performed two-step experiments. First, we assembled two networks under the same constant force. We then switched the two networks to grow against two boundaries of different constant stiffness. Interestingly, velocity of the network pushing against the stiffer barrier fell instantly even though force on the network increased gradually and by a small amount over the short time (<15 s) of this experiment (Figure 7C). Next, we assembled two networks under two different constant forces, one high and one low. We then switched both networks to grow against the same constant stiffness barrier. In this case, the velocity of the sparse network grown under

low force immediately drops below that of the denser network, even though (1) the sparse network's velocity was initially much greater, and (2) the force the sparse network experiences during the second part of the experiment is much less than that experienced by the denser network (Figure 7D). This result can be explained by how the free energy of actin filament assembly partitions between cantilever deflection and deformation of the network. In constant stiffness mode, the network and cantilever act as two springs in series. When the cantilever mode switches from constant force to constant stiffness, the force immediately rises above the critical force of the network (the original growth force) and, therefore, actin assembly begins to both deflect the cantilever and to crush older parts of the network. This partitioning immediately reduces the growth velocity.

To test our understanding of this energy partitioning within the network, we used several known parameters—network elasticity (Figure 4E), growth velocity under constant force (Figures 7C and 7D), and cantilever spring constant, to calculate the growth velocity expected at the moment of switching from constant force to constant stiffness (Supplemental Experimental Procedures). These calculated values agree well with measured velocities (dashed lines in Figures 7C and 7D) demonstrating how the instantaneous (but not the steady-state) growth velocity of branched actin networks depends on loading history. This complex dependence manifests in the different height changes of branched networks growing under constant stiffness barriers (Figure 7E) and in the force-velocity relationships calculated from them (Figure 7F). The steady-state velocities measured under constant force define the upper bound on growth rates at all forces (Figure 7F, blue dashed line). In contrast, the steadily increasing forces experienced during growth against an elastic barrier create a time-varying loading history and produce not one but a family of force-velocity relationships that define the “motor activity” of branched actin networks.

DISCUSSION

The present study demonstrates that force plays a major role in defining the architecture, mechanics, and function of branched actin networks. Specifically, we identified an intrinsic force-feedback mechanism by which load forces experienced during self-assembly increase filament density and make growing networks stiffer and more resistant to mechanical failure. Importantly, the change in mechanical properties associated with increased filament density does not obey scaling relationships that describe isotropic crosslinked or entangled actin gels.

Average Filament Length Is Invariant under Load

Elongation of actin filaments slows dramatically under load, but this slowing has no effect on the average length of filaments in a self-assembling branched network. The reason is that filament capping responds to force in the same way as filament elongation. Individual filaments grow slower under load, but because capping is also slower, they grow for a proportionally longer time, reaching the same length. The force-invariance of filament length has important consequences for the material properties of branched actin networks. If, for example, filament length decreased with applied force, the overall coherence of the

network would decrease due to loss of entanglement between branched filament arbors. Conversely, a force-induced *increase* in average filament length would produce filaments that buckle more easily under lower forces. Either response would nudge the material properties of the network toward a regime that is less capable of resisting the applied load.

Force Alters Internal Architecture of Branched Actin Networks

Over the range from zero load to forces that stall network growth, the filament density of a branched actin network increases by about an order of magnitude. A force-dependent increase in the number of free barbed ends (T.-D.L., P.B., D.M., and D.F., unpublished data) accounts for part of this increase in density (~3.5-fold), while the remainder (~3-fold) must reflect changes in filament packing. This is most easily visualized in terms of the angle between the filaments and the boundary surface they push against. In the absence of strong forces opposing growth, filaments in branched actin networks *in vivo* (Svitkina and Borisy, 1999; Weichsel et al., 2012), *in vitro* (Cameron et al., 2001), and *in silico* (Maly and Borisy, 2001; Schaus et al., 2007) are distributed symmetrically around an average angle of ~54° with respect to the membrane. This angle of attack is determined primarily by the geometry of ~72° y-branches made by the Arp2/3 complex. A 3-fold increase in filament density could be produced by a 3-fold decrease in the sine of the average angle of attack: from ~54° to ~16°. This shallower angle of attack could be produced by bending filaments or branch-points or by increasing the out-of-plane rotation of y-branches with respect to the membrane.

Branched Actin Networks Exhibit Unique Material Properties Distinct from Those of Isotropic Actin Gels

The elastic modulus of branched actin networks scales more weakly with density ($\sim c_A^{0.6}$) compared to isotropic gels ($\sim c_A^2$) and their response to test load (“pre-stress”) does not follow a “universal” scaling law. The stress-stiffening of isotropic actin networks has shown to be dominated by the entropy of individual filaments under tension (MacKintosh et al., 1995). Our data, however, indicate that the mechanics of anisotropic, branched actin networks assembled under load are determined by different microscopic processes. Instead of the entropic elasticity of long filaments, the higher stiffness and weaker dependence on density might reflect direct bending of short, stiff filaments constrained by the branched network architecture. Higher order phenomena, such as the interlocking of meso-scale arbors of branched filaments, may also contribute under these conditions. New theoretical approaches to actin mechanics will help resolve these questions.

Crosslinkers Have Different Effects on Branched Actin Network Material Properties

Differences in affinity and in network micro-architecture likely explain the differential effects of α -actinin and filamin A on sparse and dense branched actin networks. Filamin-A is a v-shape crosslinker that prefers actin filaments that cross orthogonally. α -Actinin, on the other hand, is a rod-shaped, anti-parallel dimer that can drive formation of gels or bundles. Under low load

forces, we suggest that the crossing angle between filaments from adjoining arbors will be $\sim 72^\circ$, an angle determined by the geometry of Arp2/3-dependent branching and that favors binding of filamin A. As the geometry of the network changes under load filaments from adjacent arbors intersect at higher angles, approaching 180° (anti-parallel), a configuration that disfavors filamin A but not α -actinin. This might explain why, at low growth forces the incorporation of α -actinin has a modest effect compared to filamin-A, while at high growth forces the effect of α -actinin becomes more significant.

Motor Activity of Branched Actin Networks Depends on Loading History

Mechanical failure of actin networks may be an important element of their adaptation to mechanical loading. When the load on a growing network increases, newly formed material will be denser and stronger than older layers, which are crushed by the higher load forces. Plastic deformation of weaker layers reduces their contribution to the composite stiffness of the material and transiently reduces network expansion. Understanding the combined effects of force on assembly and mechanical collapse is essential to understanding how branched actin networks push against their cellular loads. Force-mediated coupling between filament assembly and material properties represents a key difference between the motor activity of branched networks and motor proteins such as myosin or kinesin. Under a given set of biochemical conditions, the activity of a motor protein is defined by a single force-velocity curve (Carter and Cross, 2005), whereas the motor activity of branched networks exhibits a spectrum of force-velocity relationships that depend on both the instantaneous internal stiffness of the network and the external stiffness of the material against which it pushes.

EXPERIMENTAL PROCEDURES

Four main techniques are utilized in this paper: (1) reconstitution of branched networks from purified proteins (actin, profilin, Arp2/3, CP, and NPF), (2) biochemical surface micro-patterning of NPFs on coverslips, (3) atomic force microscopy to control the mechanical loading and to measure the material properties of the network, and (4) fluorescence microscopy (confocal, TIRF, and 3D STORM) of protein assembly in the network at bulk and single-molecule levels. After immersing the NPF patterned surface (technique 1) in assembly mix ($5 \mu\text{M}$ actin, $5 \mu\text{M}$ profilin, 100nM Arp2/3, 100nM CP), branched networks grew (technique 2) under loads imposed by the AFM (technique 3) and molecular assembly was observed by fluorescence microscopy (technique 4). This experimental approach allowed us to quantify the effects of force on branched network growth. We simultaneously measured mechanical properties and fluorescence intensities of branched actin networks that were grown under biochemically and mechanically defined conditions. For complete experimental details, see the *Supplemental Experimental Procedures*.

Surface Micro-patterning

We coated the coverslip with a high density of diamino-polyethylene glycol (PEG), which was derivatized with maleimide. We then photo-eliminated maleimide groups in selected regions of the coverslip by UV irradiation through a photo mask, leaving square regions ($14 \times 14 \mu\text{m}^2$ if not indicated otherwise) of intact maleimide. Unlike previous approaches (Reymann et al., 2010), our patterning method does not remove PEG molecules from the coverslip and therefore leaves the surface passivated. We reacted the intact maleimide regions with a WAVE1 mutant (WAVE1 Δ N), which replaced the N-terminal SH1 domain by mCherry and contained a single reactive cysteine residue at its

N terminus. This immobilizes the NPF in an oriented and mechanically stable manner.

Atomic Force Microscopy

To tightly couple the cantilevers to the network, we designed a custom cantilever holder to reduce the angle of the cantilever on glass substrate surface and coated cantilevers with a peptide from the filament-binding protein Ezrin. With these modifications, we never observed slippage between the cantilever and the network and, under loading conditions used in this study, we never observed the entire network macroscopically bend or buckle under the cantilever.

SUPPLEMENTAL INFORMATION

Supplemental Information includes Supplemental Experimental Procedures, seven figures, and three movies and can be found with this article online at <http://dx.doi.org/10.1016/j.cell.2015.11.057>.

AUTHOR CONTRIBUTIONS

P.B. and T.-D.L. designed and performed experiments and wrote the manuscript. P.B. purified the proteins and analyzed fluorescence data. T.-D.L. developed the AFMs and analyzed mechanical data. P.B., T.-D.L., and P.J. developed the biochemical surface micro-patterning. J.W. developed software for the analysis of single-molecule data. R.M. and B.H. designed and built the 3D-STORM. R.M. analyzed STORM data. D.A.F. and R.D.M. conceived and supervised the project and wrote the manuscript.

ACKNOWLEDGMENTS

We thank Scott Hansen for reagents, discussions, and comments on the manuscript; Thomas Surrey, Michael Vahey, and Marcus Taylor for comments on the manuscript; and members of the D.A.F. and R.D.M. labs for discussions. This work was supported by NIH R01 GM074751 (D.A.F.), NIH R01 GM061010 (R.D.M.), HHMI (R.D.M.), HFSP LT-000843/2010 (P.B.), and EMBO ALTF 854-2009 (P.B.). T.-D.L. was supported by the Taiwan National Science Council. This project was an equal collaboration between the laboratories of D.A.F. and R.D.M. The order in which the corresponding authors are listed was determined by flipping a coin.

Received: July 21, 2015

Revised: November 12, 2015

Accepted: November 23, 2015

Published: January 14, 2016

REFERENCES

- Akin, O., and Mullins, R.D. (2008). Capping protein increases the rate of actin-based motility by promoting filament nucleation by the Arp2/3 complex. *Cell* **133**, 841–851.
- Beltzner, C.C., and Pollard, T.D. (2008). Pathway of actin filament branch formation by Arp2/3 complex. *J. Biol. Chem.* **283**, 7135–7144.
- Bisi, S., Disanza, A., Malinverno, C., Frittoli, E., Palamidessi, A., and Scita, G. (2013). Membrane and actin dynamics interplay at lamellipodia leading edge. *Curr. Opin. Cell Biol.* **25**, 565–573.
- Cameron, L.A., Svitkina, T.M., Vignjevic, D., Theriot, J.A., and Borisy, G.G. (2001). Dendritic organization of actin comet tails. *Curr. Biol.* **11**, 130–135.
- Carter, N.J., and Cross, R.A. (2005). Mechanics of the kinesin step. *Nature* **435**, 308–312.
- Chaudhuri, O., Parekh, S.H., and Fletcher, D.A. (2007). Reversible stress softening of actin networks. *Nature* **445**, 295–298.
- Clark, A.G., Miller, A.L., Vaughan, E., Yu, H.-Y.E., Penkert, R., and Bement, W.M. (2009). Integration of single and multicellular wound responses. *Curr. Biol.* **19**, 1389–1395.

- Flanagan, L.A., Chou, J., Falet, H., Neujahr, R., Hartwig, J.H., and Stossel, T.P. (2001). Filamin A, the Arp2/3 complex, and the morphology and function of cortical actin filaments in human melanoma cells. *J. Cell Biol.* 155, 511–517.
- Fletcher, D.A., and Mullins, R.D. (2010). Cell mechanics and the cytoskeleton. *Nature* 463, 485–492.
- Fourniol, F.J., Li, T.-D., Bieling, P., Mullins, R.D., Fletcher, D.A., and Surrey, T. (2014). Micropattern-guided assembly of overlapping pairs of dynamic microtubules. *Methods Enzymol.* 540, 339–360.
- Gardel, M.L., Valentine, M.T., Crocker, J.C., Bausch, A.R., and Weitz, D.A. (2003). Microrheology of entangled F-actin solutions. *Phys. Rev. Lett.* 91, 158302.
- Gardel, M.L., Shin, J.H., MacKintosh, F.C., Mahadevan, L., Matsudaira, P., and Weitz, D.A. (2004a). Elastic behavior of cross-linked and bundled actin networks. *Science* 304, 1301–1305.
- Gardel, M.L., Shin, J.H., MacKintosh, F.C., Mahadevan, L., Matsudaira, P.A., and Weitz, D.A. (2004b). Scaling of F-actin network rheology to probe single filament elasticity and dynamics. *Phys. Rev. Lett.* 93, 188102.
- Gardel, M.L., Nakamura, F., Hartwig, J.H., Crocker, J.C., Stossel, T.P., and Weitz, D.A. (2006). Prestressed F-actin networks cross-linked by hinged filamins replicate mechanical properties of cells. *Proc. Natl. Acad. Sci. USA* 103, 1762–1767.
- Gardel, M.L., Sabass, B., Ji, L., Danuser, G., Schwarz, U.S., and Waterman, C.M. (2008). Traction stress in focal adhesions correlates biphasically with actin retrograde flow speed. *J. Cell Biol.* 183, 999–1005.
- Hill, T.L., and Kirschner, M.W. (1982). Bioenergetics and kinetics of microtubule and actin filament assembly-disassembly. *Int. Rev. Cytol.* 78, 1–125.
- Huang, B., Wang, W., Bates, M., and Zhuang, X. (2008). Three-dimensional super-resolution imaging by stochastic optical reconstruction microscopy. *Science* 319, 810–813.
- Insall, R.H., and Machesky, L.M. (2009). Actin dynamics at the leading edge: from simple machinery to complex networks. *Dev. Cell* 17, 310–322.
- Janmey, P.A., and McCulloch, C.A. (2007). Cell mechanics: integrating cell responses to mechanical stimuli. *Annu. Rev. Biomed. Eng.* 9, 1–34.
- Janmey, P.A., Euteneuer, U., Traub, P., and Schliwa, M. (1991). Viscoelastic properties of vimentin compared with other filamentous biopolymer networks. *J. Cell Biol.* 113, 155–160.
- Kasza, K.E., Rowat, A.C., Liu, J., Angelini, T.E., Brangwynne, C.P., Koenderink, G.H., and Weitz, D.A. (2007). The cell as a material. *Curr. Opin. Cell Biol.* 19, 101–107.
- MacKintosh, F.C., Käs, J., and Janmey, P.A. (1995). Elasticity of semiflexible biopolymer networks. *Phys. Rev. Lett.* 75, 4425–4428.
- Maly, I.V., and Borisy, G.G. (2001). Self-organization of a propulsive actin network as an evolutionary process. *Proc. Natl. Acad. Sci. USA* 98, 11324–11329.
- Marcy, Y., Prost, J., Carlier, M.-F., and Sykes, C. (2004). Forces generated during actin-based propulsion: a direct measurement by micromanipulation. *Proc. Natl. Acad. Sci. USA* 101, 5992–5997.
- Mogilner, A., and Oster, G. (1996). Cell motility driven by actin polymerization. *Biophys. J.* 71, 3030–3045.
- Mooren, O.L., Galletta, B.J., and Cooper, J.A. (2012). Roles for actin assembly in endocytosis. *Annu. Rev. Biochem.* 81, 661–686.
- Mullins, R.D., Heuser, J.A., and Pollard, T.D. (1998). The interaction of Arp2/3 complex with actin: nucleation, high affinity pointed end capping, and formation of branching networks of filaments. *Proc. Natl. Acad. Sci. USA* 95, 6181–6186.
- Nakamura, F., Osborn, E., Janmey, P.A., and Stossel, T.P. (2002). Comparison of filamin A-induced cross-linking and Arp2/3 complex-mediated branching on the mechanics of actin filaments. *J. Biol. Chem.* 277, 9148–9154.
- Nakamura, F., Osborn, T.M., Hartemink, C.A., Hartwig, J.H., and Stossel, T.P. (2007). Structural basis of filamin A functions. *J. Cell Biol.* 179, 1011–1025.
- Pantaloni, D., and Carlier, M.F. (1993). How profilin promotes actin filament assembly in the presence of thymosin beta 4. *Cell* 75, 1007–1014.
- Parekh, S.H., Chaudhuri, O., Theriot, J.A., and Fletcher, D.A. (2005). Loading history determines the velocity of actin-network growth. *Nat. Cell Biol.* 7, 1219–1223.
- Peskin, C.S., Odell, G.M., and Oster, G.F. (1993). Cellular motions and thermal fluctuations: the Brownian ratchet. *Biophys. J.* 65, 316–324.
- Pollard, T.D., and Cooper, J.A. (2009). Actin, a central player in cell shape and movement. *Science* 326, 1208–1212.
- Prass, M., Jacobson, K., Mogilner, A., and Radmacher, M. (2006). Direct measurement of the lamellipodial protrusive force in a migrating cell. *J. Cell Biol.* 174, 767–772.
- Pujol, T., du Roure, O., Fermigier, M., and Heuvingh, J. (2012). Impact of branching on the elasticity of actin networks. *Proc. Natl. Acad. Sci. USA* 109, 10364–10369.
- Renkawitz, J., Schumann, K., Weber, M., Lämmermann, T., Pflicke, H., Piel, M., Polleux, J., Spatz, J.P., and Sixt, M. (2009). Adaptive force transmission in amoeboid cell migration. *Nat. Cell Biol.* 11, 1438–1443.
- Reymann, A.-C., Martiel, J.-L., Cambier, T., Blanchoin, L., Boujemaa-Paterski, R., and Théry, M. (2010). Nucleation geometry governs ordered actin networks structures. *Nat. Mater.* 9, 827–832.
- Reymann, A.-C., Suarez, C., Guérin, C., Martiel, J.-L., Staiger, C.J., Blanchoin, L., and Boujemaa-Paterski, R. (2011). Turnover of branched actin filament networks by stochastic fragmentation with ADF/cofilin. *Mol. Biol. Cell* 22, 2541–2550.
- Schafer, D.A., Jennings, P.B., and Cooper, J.A. (1996). Dynamics of capping protein and actin assembly in vitro: uncapping barbed ends by polyphosphoinositides. *J. Cell Biol.* 135, 169–179.
- Schaus, T.E., Taylor, E.W., and Borisy, G.G. (2007). Self-organization of actin filament orientation in the dendritic-nucleation/array-treadmilling model. *Proc. Natl. Acad. Sci. USA* 104, 7086–7091.
- Storm, C., Pastore, J.J., MacKintosh, F.C., Lubensky, T.C., and Janmey, P.A. (2005). Nonlinear elasticity in biological gels. *Nature* 435, 191–194.
- Stricker, J., Falzone, T., and Gardel, M.L. (2010). Mechanics of the F-actin cytoskeleton. *J. Biomech.* 43, 9–14.
- Svitkina, T.M., and Borisy, G.G. (1999). Arp2/3 complex and actin depolymerizing factor/cofilin in dendritic organization and treadmilling of actin filament array in lamellipodia. *J. Cell Biol.* 145, 1009–1026.
- Tilney, L.G., Bonder, E.M., Coluccio, L.M., and Mooseker, M.S. (1983). Actin from Thyone sperm assembles on only one end of an actin filament: a behavior regulated by profilin. *J. Cell Biol.* 97, 112–124.
- Vinzenz, M., Nemethova, M., Schur, F., Mueller, J., Narita, A., Urban, E., Winkler, C., Schmeiser, C., Koestler, S.A., Rottner, K., et al. (2012). Actin branching in the initiation and maintenance of lamellipodia. *J. Cell Sci.* 125, 2775–2785.
- Wachsstock, D.H., Schwartz, W.H., and Pollard, T.D. (1993). Affinity of alpha-actinin for actin determines the structure and mechanical properties of actin filament gels. *Biophys. J.* 65, 205–214.
- Wagner, B., Tharmann, R., Haase, I., Fischer, M., and Bausch, A.R. (2006). Cytoskeletal polymer networks: the molecular structure of cross-linkers determines macroscopic properties. *Proc. Natl. Acad. Sci. USA* 103, 13974–13978.
- Weichsel, J., Urban, E., Small, J.V., and Schwarz, U.S. (2012). Reconstructing the orientation distribution of actin filaments in the lamellipodium of migrating keratocytes from electron microscopy tomography data. *Cytometry A* 81, 496–507.
- Welch, M.D., and Way, M. (2013). Arp2/3-mediated actin-based motility: a tail of pathogen abuse. *Cell Host Microbe* 14, 242–255.
- Wu, C., Asokan, S.B., Berginski, M.E., Haynes, E.M., Sharpless, N.E., Griffith, J.D., Gomez, S.M., and Bear, J.E. (2012). Arp2/3 is critical for lamellipodia and response to extracellular matrix cues but is dispensable for chemotaxis. *Cell* 148, 973–987.
- Yamaguchi, H., Lorenz, M., Kempf, S., Sarmiento, C., Coniglio, S., Symons, M., Segall, J., Eddy, R., Miki, H., Takenawa, T., and Condeelis, J. (2005). Molecular mechanisms of invadopodium formation: the role of the N-WASP-Arp2/3 complex pathway and cofilin. *J. Cell Biol.* 168, 441–452.

Supplemental Figures

Cell

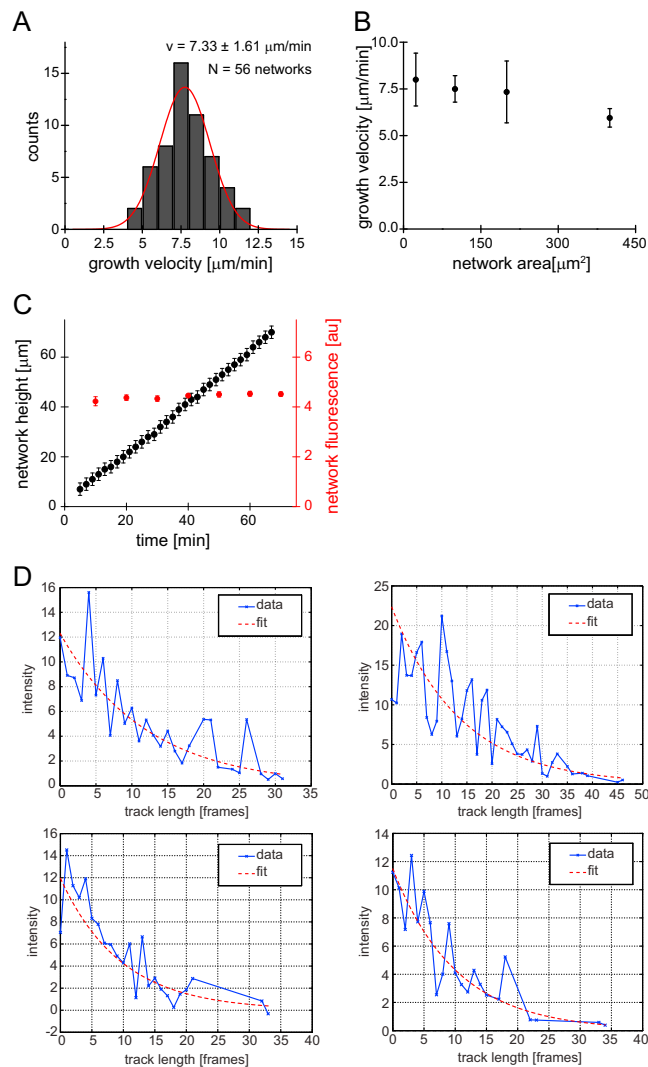


Figure S1. Dendritic Network Assembly in the Absence of Force, Related to Figure 1

- (A) Distribution of network growth velocities in the absence of load as determined by confocal microscopy for 56 networks from 12 independent experiments. The red line is a fit to a Gaussian function.
- (B) Mean network growth velocity as a function of network area. Each point contains data from at least 10 networks for 2 independent experiments.
- (C) Network height and actin network fluorescence as a function of time for networks grown at reduced profilin-actin concentrations (1.5 μM each). Data are from 6 networks. Error bars are SD.
- (D) Representative intensity traces (blue) for individual Alexa647-labeled actin molecules incorporated into a growing dendritic network loaded with 25pN/ μm^2 stress. The red dashed lines are fits to an exponential decay function $I(t) = I_0 e^{-kt}$ with I_0 = intensity at $t = 0$ and k = decay constant.

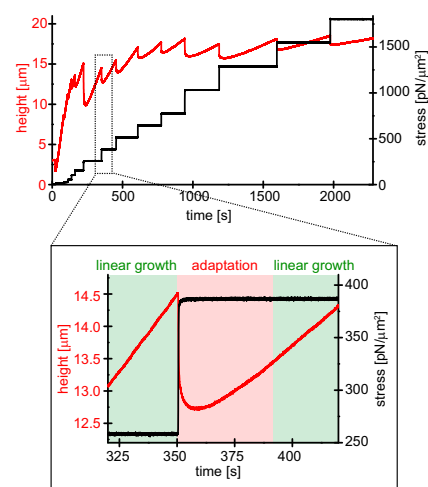


Figure S2. Dendritic Network Growth by Atomic Force Microscopy, Related to Figure 2

Height (red) and stress (black) as a function of time for a representative growing network. The stress was kept constant at a defined setpoint via the feedback mechanism of the AFM (“force-clamp mode”) until the height change over time appeared linear (inset, green area). The stress was then raised to a higher setpoint, to which the network responded by an adaptation phase (inset, red area) which was followed by a linear phase after reaching equilibrium. Network growth velocities and densities of components as a function of growth stress were determined from the linear, steady-state phases.

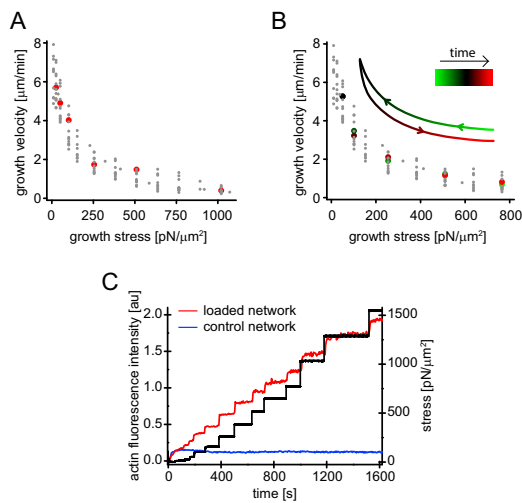


Figure S3. Network Growth Velocity Is Not Dependent on Loading-History, but Actin Polymer Density Increases in Response to Load, Related to Figure 2

(A) Force dependence of growth velocity determined for networks grown under either a single, constant stress (red) or incrementally increasing growth stresses as mostly used throughout the manuscript (gray). Both methods yield similar growth velocities.

(B) Hysteresis test. Networks are subjected to a stress cycle, going from high to low load first (green symbols) and then back (red symbols). Note that growth velocities from the descending and ascending phase are very similar to each other and to velocities measured for steadily and gradually increasing stresses (gray).

(C) Actin fluorescence for a network (red) loaded at indicated stress (black) and an adjacent, unloaded control (blue) as a function of time.

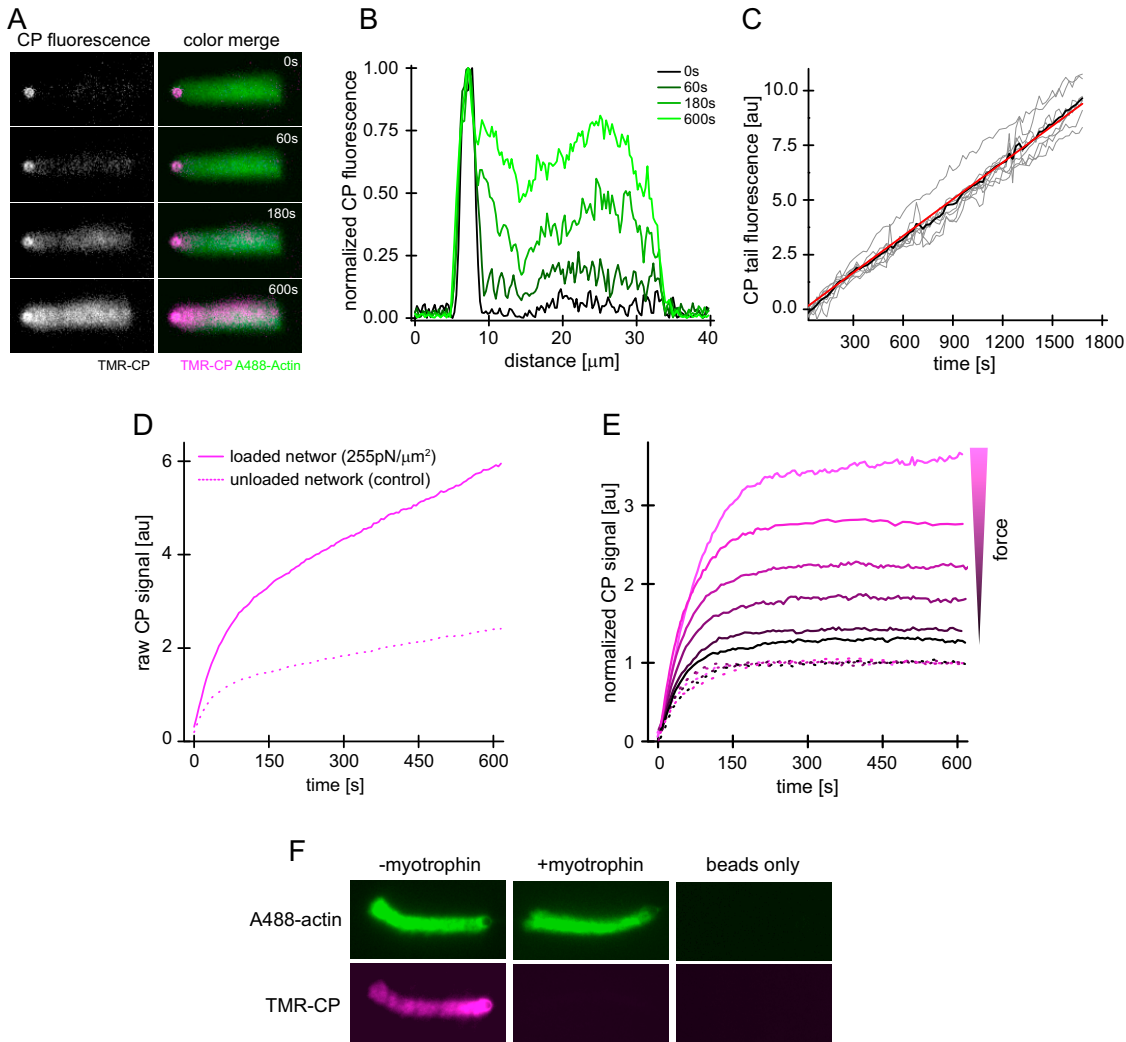


Figure S4. An ‘Arrest and Label’ Assay for the Quantification of Free Barbed Ends, Related to Figure 3

(A) Images from time-lapse widefield fluorescence microscopy of comet-tail networks assembled from NPF-coated polystyrene beads at indicated times after kinetic arrest with LatrunculinB, phalloidin and TMR-labeled CP. $t = 0$ is the start of time-lapse imaging which was about 30–60 s after biochemical arrest. Note the rapid appearance of a bead-proximal CP signal followed by the gradual accumulation of CP throughout the rest of the actin network. We interpret the first, rapid signal as capping of existing free barbed ends in the proximity to the NPF, whereas the gradual accumulation represents turnover.

(B) Normalized TMR CP fluorescence from line-scans across the comet tail along the axis of growth (front to rear = left to right) at indicated time after the beginning of imaging. Bead-proximal free ends are capped rapidly, whereas accumulation of labeled CP in the tail is gradual and slow.

(C) Kinetics of CP turnover in the comet tail for 10 individual networks (gray lines). The black line is the averaged signal and the red line is a linear fit. Note that turnover kinetics are slow and can be assumed to be linear over times $< 1500\text{s}$.

(D) Raw TMR-CP signal for dendritic networks grown from NPF-micropatterns either at $510\text{pN}/\mu\text{m}^2$ stress (continuous line) or in the absence of load (dashed line) as a function of time after kinetic arrest. The signal was fitted to a sum of an exponential and a linear function (with the exponential phase representing capping of existing free ends and the linear phase representing turnover of capped ends, see [Experimental Procedures](#)). Subtraction of the turnover signal and normalization to the unloaded internal control yields the normalized barbed end signal.

(E) The barbed end signal as a function of time for representative networks loaded with increasing load (25, 102, 255, 510, 765 and $1020\text{pN}/\mu\text{m}^2$, continuous lines) normalized to the internal, unloaded control network (dotted lines).

(F) TMR-CP fluorescence (magenta) accumulated in actin comet tails (green) 45min after kinetic arrest in the presence (middle panels) or absence (left panels) of myotrophin (a strong competitive CP inhibitor). The right panels represent a negative control for NPF-coated beads without an actin network. Note that CP does not localize to the NPF beads alone and that CP binding to the actin network is potently inhibited by myotrophin.

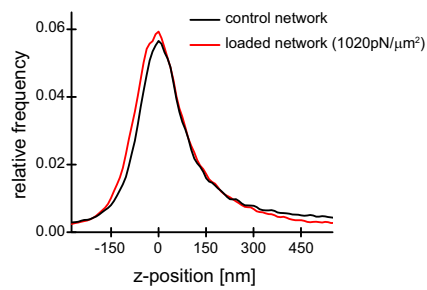


Figure S5. Axial Localization of Free Ends by STORM, Related to Figure 3

Relative frequency of barbed end localization as a function of z-position for either a representative network loaded with $1020\text{pN}/\mu\text{m}^2$ (red) or an unloaded control (black). The position is set to $z = 0$ at the maximal relative frequency.

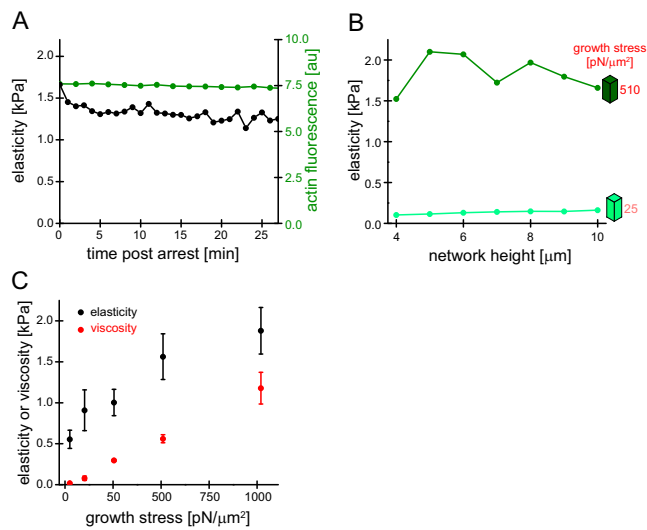


Figure S6. Dendritic Networks Are Stable after Kinetic Arrest, Related to Figure 4

(A) Network elasticity and actin fluorescence as a function of time after kinetic arrest by addition of LatrunculinB.

(B) Network elasticity during the assembly phase at 25 $\text{pN}/\mu\text{m}^2$ (light green) or 510 $\text{pN}/\mu\text{m}^2$ (dark green) as a function of sample height, showing that elasticity is nearly constant with network height. Elasticity measurements below 4 μm sample height were not reliable, because of the hydrodynamic influence of the proximal coverslip surface on the AFM cantilever.

(C) Initial elastic (black) and viscous modulus (red) from microrheology as a function of growth stress. Measurements were performed at low test load (12.5–25 $\text{pN}/\mu\text{m}^2$) following the arrest of network assembly.

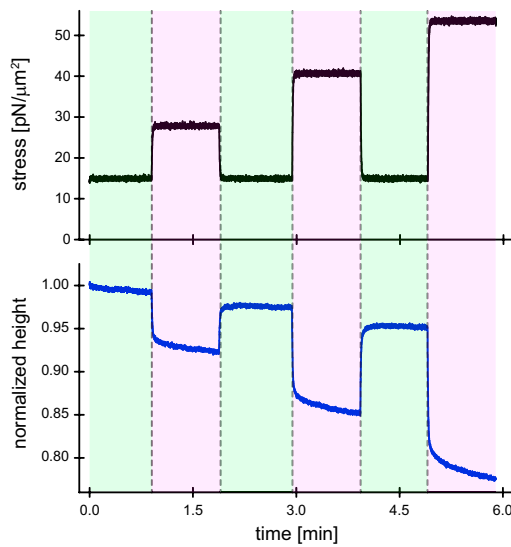


Figure S7. Application of Test Load Cycles to Dendritic Networks, Related to Figure 4

Representative force and height traces for dendritic networks subjected to test load cycles. Applied test load (black, upper panel) and resulting normalized network height (blue, lower panel) for a network assembled under $25 \text{ pN}/\mu\text{m}^2$ growth stress. Test loads are applied in form of alternating steps of increasing stress (magenta area) intermitted with recovery steps at a constant low test load (green area).

Cell

Supplemental Information

**Force feedback controls motor activity
and mechanical properties of self-assembling
branched actin networks**

**Peter Bieling, Tai-De Li, Julian Weichsel, Ryan McGorty, Pamela Jreij, Bo Huang, Daniel
A. Fletcher and R. Dyche Mullins**

Supplementary Materials and Methods:

1. Protein biochemistry:

1.1 Coverslip-immobilized proteins (NPFs and mCherry variants): The coding sequence of Human WAVE1 lacking the N-terminal SH1 domain (AA 171-559, WAVE1 Δ N) was codon-optimized for expression in E. Coli (GeneArt) and fused to an N-terminal mCherry-tag harboring an N-terminal Lys-Cys-Lys-(KCK)-tag (for surface immobilization) followed by a His₁₀-tag (for purification) and cloned into a modified pET vector containing a TEV-cleavable z-tag. To prevent surface attachment via protein sites other than the N-terminal KCK-tag, endogenous Cysteine residues of WAVE1 (Cys 296 and 407) were replaced with Serine without affecting protein activity. A non-fluorescent version of this mCherry-NPF fusion construct was generated by introducing a Tyr71->Ser mutation in mCherry (darkCherry) to facilitate multicolor TIRF microscopy when direct visualization of the NPF was not necessary. For the purification of mCherry or dark mCherry lacking NPF activity, we introduced a STOP codon between the Cherry and NPF moiety. Proteins were expressed in E.Coli (Star pRARE) for 16h at 18°C and purified by IMAC over a HiTrap Chelatin column, followed overnight TEV cleavage on ice, ion-exchange chromatography over a Source Q (XK 16-20) column and gelfiltration over a HiLoad Superdex 200 column. Proteins were SNAP-frozen in liquid nitrogen in storage buffer (20mM HEPES (pH=7.5), 150mM NaCl, 0.5mM TCEP, 0.1mM EDTA, 20% Glycerol).

1.2 Actin: Native, cytoplasmic actin from Amoeba castellanii was purified by ion-exchange chromatography and a cycle of polymerization-depolymerization as described previously (Hansen et al., 2013) and stored in filamentous form dialyzing against polymerization buffer (20mM Imidazole (pH=7.0), 50mM KCl, 1.5mM MgCl₂, 1mM EGTA, 0.5mM ATP, 0.5mM TCEP). 5ml fractions of the filamentous pool were depolymerized at a time by dialyzing into G-Buffer (2mM Tris-Cl (pH=8.0), 0.1mM CaCl₂, 0.2mM ATP, 0.5mM TCEP) for 1 week, followed by gelfiltration over a HiLoad Superdex 200 (XK16-60) column. Actin was kept in monomeric form after gelfiltration at 4C for up to two months. Actin was fluorescently labeled with Alexa488-Maleimide at Cys 374 as previously described (Hansen et al., 2013). For labeling actin with Alexa405- or Atto540Q-NHS, the profilin-actin complex was formed in G-Buffer with a 1.5-fold excess of profilin. The complex was isolated by gelfiltration over a Superdex 75 column in labeling buffer (2mM HEPES (pH=8.0), 0.1mM CaCl₂, 0.2mM ATP, 0.5mM TCEP), concentrated and labeled at reactive lysine residues by incubating with a 10-fold excess of the NHS-dye for 1h on ice. After quenching with Tris-Cl (2mM, pH=8.0), actin was polymerized by addition of 10x

polymerization buffer and a small quantity (1% of total actin) of freshly sheared filaments. After polymerization for 1h at room temperature, filaments were pelleted by ultracentrifugation (20 min at 80 krpm in a TLA100.2 rotor) and then depolymerized in G-Buffer for 1 week in the dark. Depolymerized, labeled actin was then gelfiltered over a Superdex 75 column and stored on ice.

1.3 Arp2/3 complex: The native, bovine Arp2/3 complex was purified from calf thymus glands (PelFreez) by a series of ammonium sulfate precipitation and ion-exchange chromatography (DEAE, Source Q and Source S) steps followed by gelfiltration (Superdex 200) as described previously (Doolittle et al., 2013). Arp2/3 was fluorescently labeled by addition of 3-fold excess of maleide-dye conjugate, incubated for 1.5h on ice, quenched by adding DTT to 1mM and desalted into VCA Buffer A (5mM Tris-Cl (pH=8.0), 5mM NaCl, 1mM DTT, 0.2mM MgCl₂, 0.1mM ATP). To remove a small subfraction of Arp2/3, which irreversibly bound to the NPF after labeling, the complex was bound to a 5ml NPF affinity column (N-WASP VCA immobilized on a HiTrapNHS resin) and eluted by a 10CV gradient to VCA Buffer B (5mM Tris-Cl (pH=8.0), 5mM NaCl, 0.2mM MgCl₂, 0.1mM TCEP, 0.1mM ATP). Peak fractions were pooled, concentrated and gelfiltered over a Superose 6 column. Proteins were SNAP-frozen in liquid nitrogen in storage buffer (5mM HEPES (pH=7.5), 50mM NaCl, 0.5mM MgCl₂, 0.5mM TCEP, 0.5mM EGTA, 0.1mM ATP, 20% Glycerol).

1.4 Capping protein: To generate wt CP, the α1 and β2 isoforms of murine heterodimeric capping protein were cloned into pETM20 and pETM33, respectively. To generate fluorescently tagged, wt CP, an N-terminal SNAP-tag (Keppler et al., 2003) was fused to the beta subunit. Proteins were co-expressed in E.Coli (Rosetta) for 16h at 18C and purified by IMAC over a 5ml HiTrap Chelatin column followed by overnight TEV/Precision cleavage of the N-terminal His-tags on ice. After desalting over a HiLoad Desalting column, uncleaved protein and free tags were removed by recirculation over the IMAC column. The flow through was subjected to ion-exchange chromatography over a Mono Q column and gelfiltration over a Superose 6 column. Proteins were SNAP-frozen in liquid nitrogen in storage buffer (10mM Tris-Cl (pH=7.5), 50mM NaCl, 0.5mM TCEP, 20% Glycerol). Addition of the N-terminal SNAP-tag did not affect capping activity in the absence of force as measured by polymerization of pyrene-actin in bulk or capping in single filament TIRFM assays.

1.5 Profilin: Human profilin 1 was expressed and purified as previously described (REF) and SNAP-frozen in liquid nitrogen in storage buffer (10mM Tris (pH=8.0), 50mM KCl, 1mM EDTA, 0.5mM TCEP, 20% Glycerol)

1.6 Ezrin-ABD: The C-terminus of human Ezrin (aa 553-586) followed by a 13aa Gly-rich linker and a C-terminal KCK-motif was cloned into pGEX-6P-2, expressed in E.Coli (Rosetta) for 8h at 25C, purified over a GST Trap column followed by overnight GST-Precission cleavage on ice and desalting. Desalted protein was filtered over a GST Trap column to remove free GST and GST-Precission. The flow through was gelfiltered over a Superdex 75 column and SNAP frozen in liquid nitrogen in in storage buffer (10mM Tris (pH=8.0), 150mM KCl, 0.5mM TCEP, 20% Glycerol)

1.7 Myotrophin/VI: Full length, human myotrophin was cloned into a modified pETM11 vector containing a TEV-cleavable, N-terminal His₁₀-tag and expressed in expressed in E.Coli (Rosetta) for 8h at 25C, purified over a HiTrap Chelatin column followed by overnight TEV cleavage on ice and desalting. Desalted protein was filtered over a HiTrap Chelatin column to remove free His-tag and TEV. The flow through was gelfiltered over a Superdex 200 column and SNAP frozen in liquid nitrogen in in storage buffer (20mM HEPES (pH=7.5), 150mM KCl, 0.5mM TCEP, 20% Glycerol)

2. Surface functionalization and protein immobilization:

2.1 Coverslip functionalization, photolithography and protein immobilization: Glass coverslips (22x22 mm, #1.5, high precision, Zeiss) were functionalized and patterned as described previously (Fourniol et al., 2014). Briefly, surfaces were rigorously cleaned by consecutive incubation in 3M NaOH and Piranha solution (3:2 concentrated sulfuric acid to 30% hydrogen peroxide) followed by silanization with (3-Glycidyloxypropyl)trimethoxysilane. Silanized surfaces were then passivated by reacting with diamino-PEG. Subsequently, exposed amino groups were reacted with a heterobifunctional crosslinker (BMPS) to create PEG-maleimide coated coverslips, which were subjected to UV-microlithography using a chrome-on-quartz photomasks, which selectively protected maleimide groups within chrome-covered areas from UV exposure. Micropatterned PEG-maleimide coverslips were then loosely attached to flow chambers constructed of PLL-PEG passivated microscopy counter slides and thin PDMS stripes (flow cell volume=40µl). For the immobilization of NPF on micropatterned PEG-maleimide coverslips, protein aliquots of KCK-Cherry- WAVE1ΔN (NPF) and KCK-Cherry (mock protein) were rapidly thawed and und pre-reduced with 1mM beta-mercaptoethanol for 30min on ice and then desalted twice into Immobilization Buffer (20mM HEPES (pH=7.5), 300mM NaCl, 0.5mM EDTA). Protein concentration was determined by Au_{280nm} and NPF protein mix was prepared by diluting desalted proteins to 10µM total in immobilization buffer, followed by direct incubation for 25min at room temperature with the freshly patterned PEG-maleimide coverslip in the flow cell contained in a humidified chamber. The NPF density

was controlled by adjusting the relative percentage of KCK-darkCherry-WAVE1 Δ N (NPF) and KCK-darkCherry (mock protein). Coverslips were prepared using a percentage of 60% NPF and 40% mock protein. For the FRET experiments determining the WH2 occupancy, coverslips were prepared using 50% KCK-darkCherry-WAVE1 Δ N, 10% CLPTE-darkCherry-WAVE1 Δ N (Alexa488-Cys490) and 40% KCK-darkCherry. After protein immobilization, flow cells were washed with 6 flow cell volumes wash buffer (20mM HEPES (pH=7.5), 300mM NaCl, 0.5mM EDTA, 5mM beta-mercaptoethanol), incubated for 3min to quench residual maleimide groups, washed with 6 flow cell volumes storage buffer (20mM HEPES (pH=7.5), 300mM NaCl, 0.5mM EDTA, 2mM TCEP) and stored at 4°C in a humid container for up to 5 days.

2.2 Cantilever functionalization: Tipless, uncoated cantilevers were chemically cleaned by incubating in Piranha solution (3:2 concentrated sulfuric acid to 30% hydrogen peroxide), washed, transferred to custom-built PDMS incubation chambers and functionalized by incubating for 1.5 h in Silane-PEG5000-Maleide (Nanocs, freshly resuspended to 2% (w/w) in 95% ethanol, 5% water, pH=5.0) at room temperature. The cantilevers were then washed twice in excess ethanol, dried for 1h at 75°C and washed with ultrapure water. Ezrin-ABD was diluted to 20 μ M in cantilever buffer (2mM Tris-Cl, pH=8.0) and immobilized on PEG-Maleimide-functionalized cantilevers by overnight incubation at 4C in custom-built PDMS incubation chambers. Immediately before the experiment, Ezrin-coated cantilevers were washed in excess cantilever buffers and dried.

3. Fluorescence and atomic force microscopy systems:

3.1 TIRFM-AFM system: Imaging was performed on an Observer.Z1 (Zeiss) microscope equipped with a total internal reflection fluorescence (TIRF) slider (Zeiss), a TIRF objective (PlanApochromat 100X 1.46 TIRFM, Zeiss) and a cooled charge-coupled device camera (iXon888, Andor). Fluorescence excitation was accomplished by three diode-pumped solid-state laser lines (488, 561 and 644nm), which were controlled using an acousto-optical filter and coupled into a single fiberoptic light guide (custom laser launch, Spectral Applied Research). Micro-Manager (Edelstein et al., 2010) was used to control the shutters, acousto-optical filter, dichroic mirrors and camera. Laser intensity and exposure was minimized to avoid photo-bleaching. For bulk multi-color fluorescence measurements of dendritic network component densities, images (300ms exposure time) were taken at custom intervals of increasing time (5-30s to avoid bleaching in networks growing with reduced velocity at elevated forces). Fast, one-color

imaging of single molecules was performed at an increased frame rate of 10 frames/s and a 100 ms exposure time (“streaming” mode).

Force measurements were performed using commercial AFM system (BioScope Catalyst, Bruker) which was extensively modified to a) have larger force range, b) lower the angle between the NPF-coated coverslip and the cantilever, c) prevent evaporation of aqueous solution, and d) perform micro-rheology measurements as described in detail below:

a) To increase the dynamic force range of our AFM system, we replaced the commercial AFM photodiode detector with a position sensitive detector (PSD) (Pacific Silicon Sensor, DL100-7PCBA3), which has a larger sensor area (10x10 mm²) to detect larger bending of the soft AFM cantilever. We also aligned the AFM laser close to the base of cantilever to have larger optical lever sensitivity (OLS) to gain larger cantilever bending within the detectable range of the PSD. To reduce high frequency noise, the deflection and sum signal from the PSD were processed by a low-pass filter (Krohn-Hite, 3364) with 30 Hz cut-off frequency. Custom software written in LabView (National Instruments) was used for data acquisition, force feedback, and cantilever z-position control.

b) The typical contact angle of our commercial AFM (15 degree) was too large for our experiments since it resulted in slippage of actin network on cantilever surface when applying large forces and also exerted non-uniform stress on the actin network. We therefore constructed a custom-build cantilever holder with a very low contact angle of about 3.5 degree. The conventional spring-clamp mechanism for AFM cantilever mounting on the holder is not suitable for this low-angle design. To fix AFM cantilever on the holder, we used paraffin wax (Sigma-Aldrich, 327212) as biocompatible adhesive to mount the AFM cantilever onto the low angle cantilever holder.

c) We constructed a custom sample holder that was mounted on the microscope stage to visualize dendritic networks through an inverted TIRFM microscope from the bottom and perform AFM measurements from the top. Because of the open AFM configuration leading to evaporation, we overlaid the reaction mix (150ul) with 80ul mineral oil containing a surfactant (20mg/ml Cithrol DPHS, Croda Health Care, USA) to passivate the liquid-oil interface.

d) For AFM-based microrheology measurements (Alcaraz et al., 2003; Mahaffy et al., 2000) we applied a sinusoidal wave with frequency of 2Hz and amplitude of 20 nm to the z-piezo which vertically drives the AFM cantilever. When the oscillating cantilever was in contact with the network, the cantilever normal deflection started to oscillate with the same frequency (2 Hz). The amplitude and phase shift of the oscillatory normal deflection were detected by a lock-in amplifier (7270, Signal Recovery) and used to determine the mechanical properties of the actin network.

3.2 Confocal-AFM system: Imaging was performed on an Observer.Z1 (Zeiss) microscope equipped with a confocal scanner (CSU-X1; Yokogawa Electric Corporation), a 63x objective (PlanApochromat 63X 1.4, Zeiss) and a cooled charge-coupled device camera (CascadeII, Photometrics). Fluorescence excitation by three diode-pumped solid-state laser lines (401, 488, 561 and 644nm), which were controlled using an acousto-optical filter and coupled into a single fiberoptic light guide (custom laser launch, Solamere Technology Group). Micro-Manager (Edelstein et al., 2010) was used to control the shutters, acousto-optical filter, dichroic mirrors and camera. Laser intensity and exposure was minimized to avoid photo-bleaching. Multicolor z-stacks (100ms exposure time at 0.2-1mM step sizes) were acquired at 1min time intervals. The custom AFM was constructed using a 850 nm laser (Blue Sky Research), a Position Sensitive Device (PSD, Pacific Silicon Sensor, DL100-7PCBA3), 3 piezo stages (Mad City Labs), a x-y motorized stage (Thorlabs), a manual vertical translational stage (Newport, MVN50), 3 manual translational stages (Thorlabs, MT1), a home-made cantilever holder, a home-made sample holder, and a home-made adaptor plate. The vertical linear stage was used to coarse control the AFM in z-direction. The laser, PSD, and home-made AFM cantilever holder were mounted on the vertical linear stage through 2 translational stages in x-y-, 1 translational stage in x-, and 1 piezo stage (Nano-OP100, Mad City Labs) in z-direction respectively. The home-made sample holder was mounted on the adaptor plate through x-y piezo (Nano-OP100, Mad City Labs) and x-y motorized stages for fine and coarse sample navigation in x-y-direction. The bottom of the adaptor plate is designed to fit conventional microscopy stages. During measurements, the vertical linear stage, together with all the components on it, were mounted on the confocal microscope through a custom-built adaptor plate. All the AFM electronic signals from PSD were pre-processed by an electronic filter (Krohn-Hite, 3362) set to dc low-pass at 30 Hz. Custom-written software in LabView was used for signal processing, data acquisition, and piezo stage control.

3.3 3D STORM-AFM system: The AFM system used for the 3D STORM is the same home-built AFM which is described in section 3.2. Single-molecule imaging experiments were performed on a custom-built microscope based on a Nikon Ti-U inverted microscope with an Olympus 100 \times UPlanSApo 1.4 N.A. objective and custom-built focus stabilization utilizing the reflection of an IR laser off the interface between the glass coverslip and sample. Four lasers (OBIS 405-50, OBIS 488-50, OBIS 647-120 and Sapphire 561-200-CW; Coherent) are combined with dichroic mirrors, expanded and focused to a position at the back focal plane of our objective that is controlled with a motorized stage so that the angle of the illumination light exiting the objective may vary. After the objective and tube lens the emission light passes through a cylindrical lens with a focal length of 700 mm to allow for 3D localization of individual molecules. Following the cylindrical lens a pair of relay lenses brings the image to an electron

multiplying CCD camera (Ixon+ DU897E-CS0-BV; Andor). We recorded images at a frame rate of 60 Hz with continuous 640-nm excitation for the Alexa647. Activation of Alexa647 was controlled with a 405-nm laser using a power density of less than 1 W/cm².

4. Dendritic network assembly assays:

4.1 General dendritic network assembly assay: Flow cells of micropatterned, NPF-coated coverslips were washed with twice with 250ul of ultra-pure water (Milli-Q grade) and disassembled by removal of the coverslips. Excess water was removed by a brief (5s) spin on a spin coater. Drying did not affect NPF activity if the coverslip was not kept in air for >30min. The coverslip was fixated on a custom-built sample holder by adhering to a thin PDMS O-ring and the whole assembly was transferred to the microscope stage. An ezrin-coated AFM cantilever was immobilized with a drop of hot paraffin wax on a custom built cantilever holder and then attached to the AFM head, which was mounted on the microscope and lowered to close proximity to the coverslip. 100 ml assembly buffer (20mM HEPES (pH=7.0), 100mM KCl, 20mM beta-Mercaptoethanol, 1.5mM MgCl₂, 1mM EGTA, 1mM ATP, 0.5mg/ml beta-casein, 10nM Alexa488-labelled actin) were added in between coverslip and cantilever holder. Low amounts of labelled actin were included in the buffer to visualize the NPF patterns indirectly via the binding of actin monomers. 80ul of mineral oil containing 20mg/ml Cithrol DPHS (to passivate the oil-buffer interface) was overlaid onto the buffer to seal it from air exposure. The Optical Lever Sensitivity (OLS) is characterized by measuring the force-distance curve in contact with the hard glass surface, prior to every measurement. An NPF pattern was then positioned at an axial distance of 3um directly under the AFM cantilever via the motorized stage and the x- and y-piezoelectric stage control. Actin network growth was finally initiated by addition of 50μl of network proteins in assembly buffer (final concentration: 5μM actin, 5μM profilin, 100nM Arp2/3, 100nM CP if not indicated otherwise). Synchronously, multicolor TIRFM time-lapse imaging was initiated. For bulk fluorescence, multicolor TIRFM experiments, the protein mix was supplemented with 1%Alexa488-actin, 5% Alexa647-Arp2/3 and 15% TMR-SNAP-CP. After the height of the growing network reached the cantilever (as indicated by cantilever displacement and a rise in force), the force was kept constant at a defined setpoint by engaging the force-feedback mechanism (“force-clamp mode”). The force was maintained until both network fluorescence and growth velocity reached a steady state, upon which the force was changed to a higher setpoint. This cycle was repeated until network growth was slowed to velocities <200 nm/min, close to mechanical stall. Network growth did not exhibit hysteresis, hence the order or duration by which the individual forces were applied did not affect the growth velocity (Supplemental Fig. 3).

4.2 Single molecule dendritic network assembly assay for TIRFM-AFM: Assays were carried out as described in the section 4.1 with the following exceptions: For single color, single molecule imaging, assembly buffer was supplemented with an oxygen scavenger system (40mM glucose, 125 µg/ml glucose oxidase, 40µg/ml catalase) and 2mM Trolox and the protein mix contained either 0.02% (1 in 5000) Alexa647-Arp2/3, 0.02% (1 in 5000) Alexa647-SNAP-CP or 0.000066% (1 in 1500000) Alexa647-Actin.

4.3 “Arrest and label” assay for the visualization of free barbed ends by TIRF-AFM: Assays were carried out as described in the section 4.1 with the following exceptions: Assembly buffer was supplemented with an oxygen scavenger system (40mM glucose, 125µg/ml glucose oxidase, 40µg/ml catalase) and 2mM Trolox and the protein mix contained only Alexa488-Actin (1% of total) as fluorescent label. The force was maintained a single setpoint until the network reached steady state growth and a minimum height of >5µm. Network growth was then arrested by carefully diluting the reaction (150µl total) by adding 400µl fixing buffer (assembly buffer containing Latrunculin B (15µM final), Phalloidin (15µM final) and TMR-CP (100nM final; the fraction of labelled capping after arrest was thus 100nM of 127nM total, hence 79% of total). Synchronous addition of Latrunculin and Phalloidin has previously been shown to maintain the ratio of filamentous and polymeric actin in dendritic networks (Akin and Mullins, 2008). Therefore, labeled capping protein can, after its addition, immediately bind to available free ends as well as capped ends that become uncapped during further incubation of the sample (turnover). This turnover fraction can be quantified and subtracted from the data (see section 5.3).

4.4 “Arrest and label” assay for the visualization of free barbed ends by 3D STORM-AFM: Assays were carried out as described in the previous section (4.3) with the following exceptions: Reactions were scaled down to half of the volume (75µl total in comparison to 150µl for standard conditions) and did not contain Trolox. Network growth was arrested by carefully diluting the reaction (75µl total) by adding 25µl fixing buffer (assembly buffer containing Latrunculin B (15µM final), Phalloidin (15µM final) and Alexa647-CP (30µM final). The fraction of labelled capping after arrest was therefore 30nM of 105nM total, hence 28%. This lower labeling fraction (compared to section 4.3) was required to achieve labeling densities suitable for single molecule STORM imaging. We inhibited further capping after 150s after network arrest by addition of 1ml dilution mix (assembly buffer containing Latrunculin B (1µM final), Phalloidin (1µM final), an oxygen scavenger system (40mM glucose, 125 µg/ml glucose oxidase, 40µg/ml catalase), 1mM beta-Mercaptoethanol and 3.7µM Myotrophin (competitive, high-affinity CP inhibitor (Bhattacharya et al., 2006)). The short incubation period with labeled CP after arrest (150s) was

sufficient for the near complete capping of all free ends (Supplemental Fig. 4), but minimized the contribution of the turnover fraction of already capped ends to the overall signal.

4.5 Measurement of network mechanical properties: After the actin network reached a height of 10 μ m, LatrunculinB (15 μ M final) was added to the reaction to terminate further actin polymerization and kinetically arrest the network. To avoid large force fluctuations during this arrest step, the AFM force clamp was transiently disengaged at the point of addition and turned back on once the vertical AFM signal stabilized. Potential drift in the vertical signal or the AFM stage during assembly and arrest was corrected for by carefully disengaging the AFM cantilever from the actin network, moving to a position away from the network and bringing it into contact with the coverslip surface to recalibrate the surface position. After 10min following kinetic arrest, the AFM cantilever was positioned back to the top of actin network. The height and the elasticity of the actin network were first measured at minimum load stress (12.5-25 pN/ μ m²). The load force was then gradually increased in form of a load cycle (Supplemental Fig. 7), with 1min long steps at the low stress 12.5-25 pN/ μ m²) alternating with 1min long steps at increasing high stresses. Actin fluorescence, sample rheology amplitude and phase as well as sample height were continuously measured during assembly of the network and the load cycles after arrest and further processed for data analysis (Section 5.8-9).

To study the growth velocity of actin network against a defined external stiffness (Fig. 7), we first grew the actin network at a constant growth force (under force clamp conditions, hence at zero external stiffness) until a height of 4um had been reached and then disengaged the force clamp. Disengaging the force clamp results in the network pushing against the defined external stiffness of the cantilever, to which we refer as stiffness clamp mode. The external stiffness was varied by using cantilevers with different force constants (0.1-0.01 N/m).

5. Data analysis:

5.1 Quantification of network growth velocity: Constant growth forces were applied to a growing network under AFM force clamp control. The growth velocity of the network was determined by the slope of height-time curve at individual constant growth forces. However after switching to a new growth force, the network needed time to adapt the new growth force to reach constant growth. Therefore the slope is not considered for growth velocity until the network reached the steady constant growth where the slope is constant.

5.2 Quantification of bulk fluorescence intensities from TIRFM and confocal imaging: The mean intensities of all network components (actin, Arp2/3, CP) from multicolor, time-lapse TIRFM images were quantified via ImageJ (ROI Manager->Multi Measure function) from square region of interests (ROIs) matching the network area. Background intensity was determined from adjacent regions (10um distance) of the same size and subtracted from the network intensity. For Arp2/3 and actin, a small (<30% of total intensity in the absence of force for TIRFM imaging, <5% for confocal imaging) fraction of fluorescence in the network area is due to binding to the NPF in addition to the actin network. The intensity of this signal was quantified during the initial lag phase preceding actin network nucleation and subtracted from the network intensity. The fluorescence intensities were plotted as a function of time together with the height of the sample as well the counterforce. Mean fluorescence intensities at were then calculated by averaging over the fluorescence signal during steady growth at a constant force. The variance in fluorescence intensity during these steady state periods was very low (SD<2% total).

5.3 Quantification of free barbed end densities from TIRFM imaging: Fluorescence intensities following network arrest and synchronous TMR-CP addition were determined as described in the previous section and plotted as function of time. Fluorescence intensity traces consisted of a rapid, exponential phase which corresponded to immediate capping of available free ends, as well as a slow, linear phase that can be attributed to slow uncapping and recapping (turnover) of capped ends throughout the dendritic network. We established in control experiments that this slow turnover can indeed be approximated to be linear over the timescale of our experiment (Supplemental Fig. 4). We thus fitted the data with a sum of an exponential and a linear function: with I_{free} being the amplitude of the rapid exponential capping phase. I_{free} is therefore a measure of the amount of free uncapped ends.

5.4 Quantification of free barbed end densities from STORM imaging: Actin networks were imaged with the STORM microscope described in section 3.3. We recorded a sequence of images with two actin networks in the frame: one without an applied force and one with a force from the AFM. Each sequence typically contained 15000 images and we recorded an image sequence at multiple focal planes including at the coverslip, 400 nm beyond the coverslip and 800 nm beyond the coverslip. For each image in a sequence, fluorescent spots were identified and fit to an elliptical Gaussian function to find their positions, intensities, widths and ellipticities. Spots too dim, wide or elliptical were discarded from further analysis. Based on the ellipticity of the fitted Gaussian function we were able to localize each molecule in z (Huang et al., 2008). In comparing the forced and unforced networks we looked at the distribution of the localized molecules' positions in z and the total number of localized molecules in each network. To correct for uneven illumination in the field of view containing the two networks which would bias the

relative number of localized molecules, we recorded multiple sequences of images containing two networks that were both unforced under identical conditions to those experiments with one forced and one unforced network. These controls allowed us to correct the number of localized molecules according to where in the image plane the network resided.

5.5 Single molecule tracking and classification: For detection and tracking of single actin, Arp2/3 and capping protein molecules in TIRF time-lapse images, we used the u-track software package (Jaqaman et al., 2008). After complete tracking, an additional step classifies tracks into productive (molecules that are incorporated into the network and continuously grow out of the TIRF microscopy field of view as indicated by a progressive drop in fluorescence intensity) or unproductive (stuck and/or blinking molecules at constant intensity and position). This is done in a semi-automated process: All individual tracks of minimum length 5 frames (= 500 ms) are randomly distributed amongst six biological experts. Each expert subsequently classifies all individual tracks of his share as productive or unproductive. In this step, 10% of all tracks are classified by two experts independently to estimate the classification uncertainty. This led to a fraction of tracks of at least 90% over all sample clips that is associated to the same class by both experts. In order to efficiently process significant amounts of microscopy data, we further automated our analysis procedure, by calculating a set of 10 feature parameters for each track. All features are based on the dynamics of intensity and position of each track. The set of features in combination with the combined classification results of the experts was used subsequently for training a supervised random forest classifier. Cross validation yielded correct classification in at least 82% of all tracks. In order to further improve this performance, we followed an active learning strategy in which borderline cases (i.e. tracks for which the decision trees in the forest do not agree well in their classification decision) are decided by an expert. Using cross validation of this semi-automated procedure, the amount of manually classified tracks is tuned to yield a comparably high correct classification performance as the group of experts (i.e. > ~90%). After classification, productive tracks are used in further analyses exclusively.

5.6 Determination of biochemical assembly rates, filament lengths and network densities from single molecule experiments: The mean event rates of productive network incorporation (in counts per network per second) was determined for all network components (actin, Arp2/3 and CP) from single molecule “spike-in” experiments at 5nN and multiplied by the respective labeling ratio to yield the total polymerization, nucleation and capping rate at this force. The average filament length (in number of monomers) at 5nN was calculated by the either ratio of the polymerization rate to the nucleation or capping rate and expressed in nm by assuming 377 actin monomers per 1000nm of filament. Filament

lengths determined by either ratio were in excellent quantitative agreement with each other, as a result of the similar nucleation and capping rates. The average network density at 5nN was determined by dividing the average polymerization rate (monomers/s) by the volume rate (product of the network area and the average growth velocity expressed as l/s) and expressed as M. The values of all these quantities determined at 5nN served as a calibration for their corresponding bulk fluorescence measurements which were carried out over the whole force regime. For instance, the normalized actin flux as a function of force (Fig. 2E) was multiplied by the polymerization rate at 5nN (Fig. 2F) to determine the polymerization rate as a function of force.

5.7 Determination of mechanical, biochemical power and energy efficiency: The mechanical power of the network was determined by the product of the network growth velocity and the external force (Fig. 2B) and expressed as $k_B T/s$. The rate of energy consumption was calculated by the product of the network polymerization rate (monomers/s per network) and the free energy change per monomer polymerized, which was determined by with $k_{on} = 4.8 \text{ s}^{-1} \mu\text{M}^{-1}$ (which was determined from single filament TIRFM polymerization experiments and found to be slightly lower for our cytoplasmic profilin-actin complex compared to literature values for muscle actin) and $k_{off} = 1 \text{ s}^{-1}$ (Kuhn and Pollard, 2005). We therefore assume a free energy change of $3.18 k_B T$ or 13.07 pN nm per monomer polymerized for our experimental conditions. The ratio of the mechanical power and the rate of energy consumption yields the dimensionless energy efficiency.

5.8 Determination of sample elasticity from microrheology measurements: Based on the definition of viscoelasticity, when a viscoelastic material is deformed by a sinusoidal compression, the elastic modulus (G') could be written as $G' = \frac{\sigma_0}{\varepsilon_0} \cos \theta$, where σ_0 and ε_0 are the amplitudes of stress and strain and θ is the phase shift between them. In our measurements, amplitude (X_0) and phase shift (θ) of the oscillatory normal deflection were detected by a lock-in amplifier. Together with the applied amplitude of z-piezo (D_0) and characterized cantilever spring constant (k), NPF pattern area (A), and network height (H), the amplitude of stress and strain of the network can be written as $\sigma_0 = \frac{X_0 k}{A}$ and $\varepsilon_0 = \frac{D_0 - X_0}{H}$. Therefore the elastic modulus is re-written as $G' = \frac{X_0 k H}{A(D_0 - X_0)} \cos \theta$. Before each measurement, the oscillating cantilever was put in contact with a hard surface to characterize the reference phase and z-piezo amplitude at different forces to obtain reference values for θ and D_0 .

5.9 Estimation of composite network elasticity: To calculate the load force-dependent total elasticity of network that grew under two different growth forces, we first calculated the spring constant of each “layer” from elasticity by $k = \frac{G'A}{H}$, where A is the cross section area, H is the thickness, and G' is the elastic modulus of that layer. With the spring constants of two layers (k_1 and k_2) in series, the total spring constant (k_{total}) follows $\frac{1}{k_{\text{total}}} = \frac{1}{k_1} + \frac{1}{k_2}$. In the final, the total elastic modulus of the whole network can be calculated by $G'_{\text{total}} = k_{\text{total}} \frac{H_{\text{total}}}{A_{\text{total}}}$, where $A_{\text{total}} = A_1 = A_2$ in our experiments. In summary, the elastic modulus of the composite network with two layers can be written as $G'_{\text{total}} = \frac{G'_1 G'_2 (H_1 + H_2)}{A_{\text{total}} (H_1 G'_2 + H_2 G'_1)}$. Please note that both G'_1 and G'_2 are load force-dependent as well as H_1 and H_2 . The initial H_1 and H_2 were characterized in each composite measurement.

5.10 Prediction of grow velocity from network and external elasticity: To calculate the growth velocity of the network after changing from force clamp mode to free deflection mode, we have to consider the elasticity of network and the spring constant of cantilever. At the moment of switching the AFM from force clamp to free deflection mode, two assumptions have to be made to predict the growth velocity after disengaging the force clamp: 1) the force applied to the network is the nearly the same is nearly the same before and right after switching off the force clamp; 2) the network and the cantilever are acting physically as two springs in series. Both of these assumptions hold for the short timescale of these experiments. Therefore the growth of network under constant force conditions ($\Delta X_{\text{force constant}}$) will be equal to the deflection of network ($\Delta X_{\text{network}}$) and cantilever ($\Delta X_{\text{cantilever}}$) in constant stiffness mode, $\Delta X_{\text{force constant}} = \Delta X_{\text{network}} + \Delta X_{\text{cantilever}}$; and force can be written as $F = \Delta X_{\text{cantilever}} k_{\text{cantilever}} = (\Delta X_{\text{cantilever}} + \Delta X_{\text{network}}) k_{\text{total}}$, where $k_{\text{total}} = \frac{k_{\text{cantilever}} k_{\text{network}}}{k_{\text{cantilever}} + k_{\text{network}}}$. Under conditions of constant external stiffness, the growth velocity is measured by the change of cantilever deflection, which is $\Delta X_{\text{cantilever}}$. By all the equations above, we can obtain $\Delta X_{\text{cantilever}} = \Delta X_{\text{force constant}} \frac{k_{\text{network}}}{k_{\text{cantilever}} + k_{\text{network}}}$. The predicted growth velocity after disengaging the force clamp can thus be obtained from $V_{\text{stiffness constant}} = V_{\text{force constant}} \frac{k_{\text{network}}}{k_{\text{cantilever}} + k_{\text{network}}}$, where the spring constant of network can be extracted by $k_{\text{network}} = \frac{G'_{\text{network}} A}{H}$ (G'_{network} , A , and H are elastic modulus, cross section area, and height of the network).

Supplementary References:

- Alcaraz, J., Buscemi, L., Grabulosa, M., Trepat, X., Fabry, B., Farré, R., and Navajas, D. (2003). Microrheology of human lung epithelial cells measured by atomic force microscopy. *Biophys. J.* *84*, 2071–2079.
- Bhattacharya, N., Ghosh, S., Sept, D., and Cooper, J.A. (2006). Binding of myotrophin/V-1 to actin-capping protein: implications for how capping protein binds to the filament barbed end. *J. Biol. Chem.* *281*, 31021–31030.
- Doolittle, L.K., Rosen, M.K., and Padrick, S.B. (2013). Purification of native Arp2/3 complex from bovine thymus. *Methods Mol. Biol.* *1046*, 231–250.
- Edelstein, A., Amodaj, N., Hoover, K., Vale, R., and Stuurman, N. (2010). Computer control of microscopes using μ Manager. *Curr Protoc Mol Biol Chapter 14*, Unit14.20.
- Fourniol, F.J., Li, T.-D., Bieling, P., Mullins, R.D., Fletcher, D.A., and Surrey, T. (2014). Micropattern-guided assembly of overlapping pairs of dynamic microtubules. *Meth. Enzymol.* *540*, 339–360.
- Hansen, S.D., Zuchero, J.B., and Mullins, R.D. (2013). Cytoplasmic actin: purification and single molecule assembly assays. *Methods Mol. Biol.* *1046*, 145–170.
- Huang, B., Wang, W., Bates, M., and Zhuang, X. (2008). Three-dimensional super-resolution imaging by stochastic optical reconstruction microscopy. *Science* *319*, 810–813.
- Jaqaman, K., Loerke, D., Mettlen, M., Kuwata, H., Grinstein, S., Schmid, S.L., and Danuser, G. (2008). Robust single-particle tracking in live-cell time-lapse sequences. *Nat. Methods* *5*, 695–702..
- Keppler, A., Gendreizig, S., Gronemeyer, T., Pick, H., Vogel, H., and Johnsson, K. (2003). A general method for the covalent labeling of fusion proteins with small molecules in vivo. *Nat. Biotechnol.* *21*, 86–89.
- Kuhn, J.R., and Pollard, T.D. (2005). Real-time measurements of actin filament polymerization by total internal reflection fluorescence microscopy. *Biophys. J.* *88*, 1387–1402.
- Mahaffy, R.E., Shih, C.K., MacKintosh, F.C., and Käs, J. (2000). Scanning probe-based frequency-dependent microrheology of polymer gels and biological cells. *Phys. Rev. Lett.* *85*, 880–883.